Tectonophysics 617 (2014) 31–43

Contents lists available at ScienceDirect

Tectonophysics

journal homepage: www.elsevier.com/locate/tecto

Polyphase exhumation in the western Qinling Mountains, China: Rapid Early Cretaceous cooling along a lithospheric-scale tear fault and pulsed Cenozoic uplift

Bianca Heberer [a,*], Thomas Anzenbacher [a], Franz Neubauer [a], Johann Genser [a], Yunpeng Dong [b], István Dunkl [c]

[a] Dept. Geography and Geology, University of Salzburg, Hellbrunnerstr. 34, A-5020 Salzburg, Austria
[b] State Key Laboratory of Continental Dynamics, Department of Geology, Northwest University, Northern Taibai Str. 229, Xi'an 710069, China
[c] Geoscience Center, University of Göttingen, Goldschmidtstrasse 3, D-37077 Göttingen, Germany

ARTICLE INFO

Article history:
Received 16 June 2013
Received in revised form 14 November 2013
Accepted 12 January 2014
Available online 22 January 2014

Keywords:
Qinling Mountain
Age–elevation-relationship
Thermochronology
Yanshanian orogeny
Tibetan Plateau uplift

ABSTRACT

The western sector of the Qinling–Dabie orogenic belt plays a key role in both Late Jurassic to Early Cretaceous "Yanshanian" intracontinental tectonics and Cenozoic lateral escape triggered by India–Asia collision. The Taibai granite in the northern Qinling Mountains is located at the westernmost tip of a Yanshanian granite belt. It consists of multiple intrusions, constrained by new Late Jurassic and Early Cretaceous U–Pb zircon ages (156 ± 3 Ma and 124 ± 1 Ma). Applying various geochronometers ($^{40}Ar/^{39}Ar$ on hornblende, biotite and K-feldspar, apatite fission-track, apatite [U–Th–Sm]/He) along a vertical profile of the Taibai Mountain refines the cooling and exhumation history. The new age constraints record the prolonged pre-Cenozoic intracontinental deformation as well as the cooling history mostly related to India–Asia collision. We detected rapid cooling for the Taibai granite from ca. 800 to 100 °C during Early Cretaceous (ca. 123 to 100 Ma) followed by a period of slow cooling from ca. 100 Ma to ca. 25 Ma, and pulsed exhumation of the low-relief Cretaceous peneplain during Cenozoic times. We interpret the Early Cretaceous rapid cooling and exhumation as a result from activity along the southern sinistral lithospheric scale tear fault of the recently postulated intracontinental subduction of the Archean/Palaeoproterozoic North China Block beneath the Alashan Block. A Late Oligocene to Early Miocene cooling phase might be triggered either by the lateral motion during India–Asia collision and/or the Pacific subduction zone. Late Miocene intensified cooling is ascribed to uplift of the Tibetan Plateau.

1. Introduction

The enigmatic Jurassic to Lower Cretaceous compressional "Yanshanian" orogenic belts (Dong et al., 2008; Enkelmann et al., 2006; Faure et al., 2012; Wong, 1927, 1929) of Central and Eastern China, which are rich in granites, are generally considered to have formed in response to geodynamic processes related to either (1) the subduction of the (Palaeo-)Pacific plate (e.g. Li and Li, 2007; Mao et al., 2010), (2) a stage of the closure of the Neotethys forming the Qiangtang orogenic belt on the Tibetan Plateau (e.g. Zhang et al., 2012), (3) the collision between Siberia and Mongolia after the closure of the Mongol–Okhotsk Ocean (e.g. Davis et al., 2001; Yin and Nie, 1993), (4) intracontinental W-directed subduction of the North China Block (NCB) underneath the Alashan Block (Faure et al., 2012) or a combination of the effects of (1) to (3), i.e. multi-directional compressional deformation caused by convergence of multiple surrounding plates toward the NCB in the center (Dong et al., 2008). Generally, an earlier compressional stage (pre-136 Ma, Yanshanian tectonics sensu stricto according to Faure et al., 2012) and a later extensional stage are distinguished. Particularly in Eastern China, Jurassic to Early Cretaceous tectonics are often related to thermal domes and metamorphic core complexes of extensional origin (Faure et al., 2012; Wu, 2005; Yang et al., 2006). Similar Jurassic to Early Cretaceous tectonic processes also affected the Qinling–Dabie orogen (Dong et al., 2011). Superimposed on these Cretaceous tectonic processes, the western part of the Qinling–Dabie orogen has also been affected by Cenozoic (since ca. 50 Ma) east-directed lateral extrusion away from the India–Asia collision zone after closure of the Neotethys Ocean (Mercier et al., 2013 and references therein; Molnar and Tapponnier, 1977). However, the detailed evolutionary history of the Qinling orogen during Cretaceous to Cenozoic times is still unclear.

In this study we present results from a multi-method thermochronological study (U–Pb on zircon, Ar–Ar on hornblende, biotite and K-feldspar, apatite fission-track (AFT), apatite (U–Th–Sm)/He (AHe) on an age–elevation profile of ca. 2500 m vertical distance of the Taibai granite, a crustal-scale footwall block in the Qinling. The aim was to extract more detailed information on both the Cretaceous and the Cenozoic cooling and denudation history by combining high- and low-T geochronometers, thus covering a wide range of crustal depths. Work focused along a vertical transect since such samples record the

* Corresponding author.

http://dx.doi.org/10.1016/j.tecto.2014.01.011
0040-1951

passage through progressively lower temperatures while samples are exhumed towards the surface. If exhumation could exhume samples from below the partial annealing/retention zones and closure depths of the respective geochronometer, then the onset of fast cooling and denudation can be directly identified by a distinct break in slope of plotted ages (Fitzgerald and Gleadow, 1990; Fitzgerald et al., 1995; Stockli et al., 2000).

We find that the Taibai granite represents the westernmost pluton of a ca. 1000 km long Yanshanian granite belt extending to the Dabie Shan (Fig. 1). Results from geochronometric dating evidence rapid post-Yanshanian cooling, followed by a ca. 75 Ma long phase of tectonic quiescence, and then pulsed cooling phases in the Cenozoic. We expand the recently proposed model of Yanshanian tectonics (Faure et al., 2012) and explain the Taibai granite as formed on the westernmost tip of a lithospheric-scale tear fault, which was later reactivated by the North Qinling fault during Cenozoic extrusion away from the Tibet plateau as a result of the collision of India with Asia.

2. Geological setting

The Qinling Mountains are part of the 2000 km long Central China orogen. They formed by the collisions between the North China, South Qinling and South China Blocks along the Shangdan suture to the north and the Mianlue suture to the south in Paleozoic and Later Triassic times, respectively (e.g. Dong et al., 2011 and references therein; Li et al., 1989; Ratschbacher et al., 2006; Zhang et al., 1989). The area underwent Late Jurassic–Early Cretaceous (=Yanshanian) shortening, associated with the intrusion of A-type granites (Dong et al., 2011). Subsequently, the area was reactivated by the Pacific back-arc extension (Engebretson et al., 1985).

Located close to the northern margin of the Qinling Mountains, the Taibai granite (Fig. 2) was supposed to be a composite Indosinian granite with a U–Pb zircon age of 216 ± Ma (Xiao et al., 2000) overprinting a foliated quartz monzonite with a Rb–Sr age of 455 Ma (Zhou et al., 1994). To the north, the North Qinling Margin fault separates the Cenozoic Weihe graben and the Qinling Mountains. The Weihe graben is part of a Cenozoic graben system surrounding the Ordos Block, a major intracratonic basin (Fig. 1). Large and sharp contrasts in lithospheric (>200 km vs. 80 km) and crustal thickness (40–50 km in general and >37 km beneath rifts) exist between the Ordos Block and the adjacent rift areas (Chen et al., 2009). Such a thick lithospheric mantle root beneath the Ordos attests that the block retained its rigidity and thickness over a long time period and exhibits features of a typical craton (Xu and Zhao, 2009). The Weihe graben exhibits a half-graben type structure along the North Qinling fault. The basin is filled with ca. 6000 m of lacustrine and alluvial deposits covered by Quaternary loess (Mercier et al., 2013 and references therein). Locally, graben development and subsidence initiated in the Mid(?)–Late Eocene to Early Oligocene. Major increases in deposition rates are observed for the Late Oligocene–Early Miocene, Late Miocene and Quaternary (Liu et al., 2013). Latest Pliocene to Quaternary extension rates are estimated at 1.6 mm/yr (Zhang et al., 1998). During Quaternary times subsidence reached a maximum value of 1 mm/yr (Bellier et al., 1988b, 1991; Mercier et al., 2013; Zhang et al., 1998). Numerous destructive earthquakes occurred within the Weihe graben, e.g. the 1556 M8 Huaxian earthquake (Zhang et al., 1995). Ground fissures and ongoing faulting indicate that this region is still tectonically active today (Li et al., 2001). Between the Qinling Mts. and the Weihe basin, mainly strike-slip movements occurred along the WNW–ESE trending North Qinling fault zone (Fig. 2), a major ductile shear zone during Palaeozoic–Mesozoic times, followed by normal and strike-slip, brittle motions during Late Cretaceous and Cenozoic (Huang and Wu, 1992; Mattauer et al., 1985).

Based on fault analyses, Mercier et al. (2013) recently proposed a complex, six-stage kinematic pattern for the North Qinling–Weihe region: Initial Late Cretaceous to Paleocene WNW–ESE extension (1) was followed by Early Eocene transpression (2) with NNE–SSW shortening, interpreted as a far-field effect of India–Asia collision. During the Mid-Eocene to Early Oligocene NE–SW extension (3) prevailed, followed by a Late Oligocene–Early Miocene second transpressional

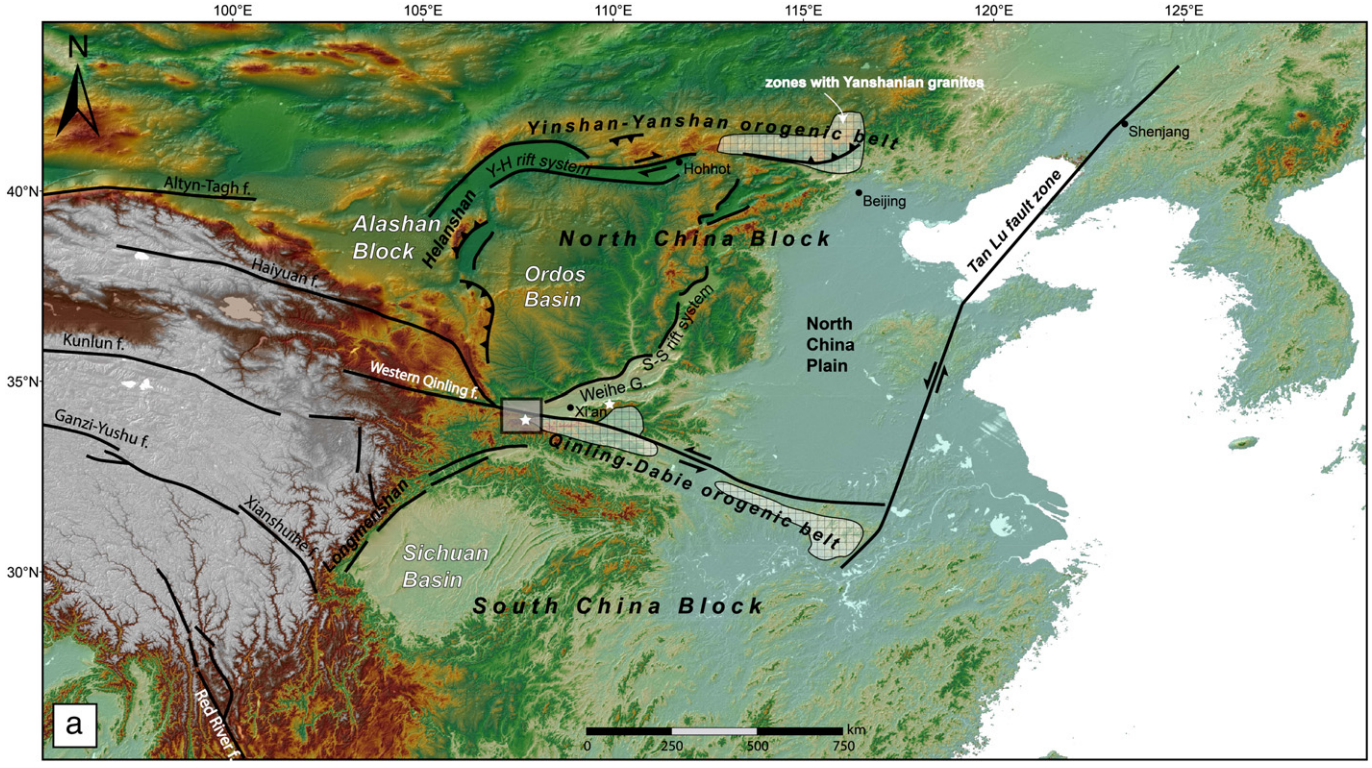

Fig. 1. (a) Digital elevation model based on SRTM data of Eastern Asia showing the major tectonic units. Y–H: Yinchuan–Hetao rift system; S–S: Shaanxi–Shanxi rift system; WG: Weihe graben. Note the location and extent of the area covered by inset b indicated by shaded box. White asterisks denote the location of the Taibai Mtn. west of Xi'an and the Hua Mtn. east of Xi'an. White cross-hatched fields indicate zones with Yanshanian granites.

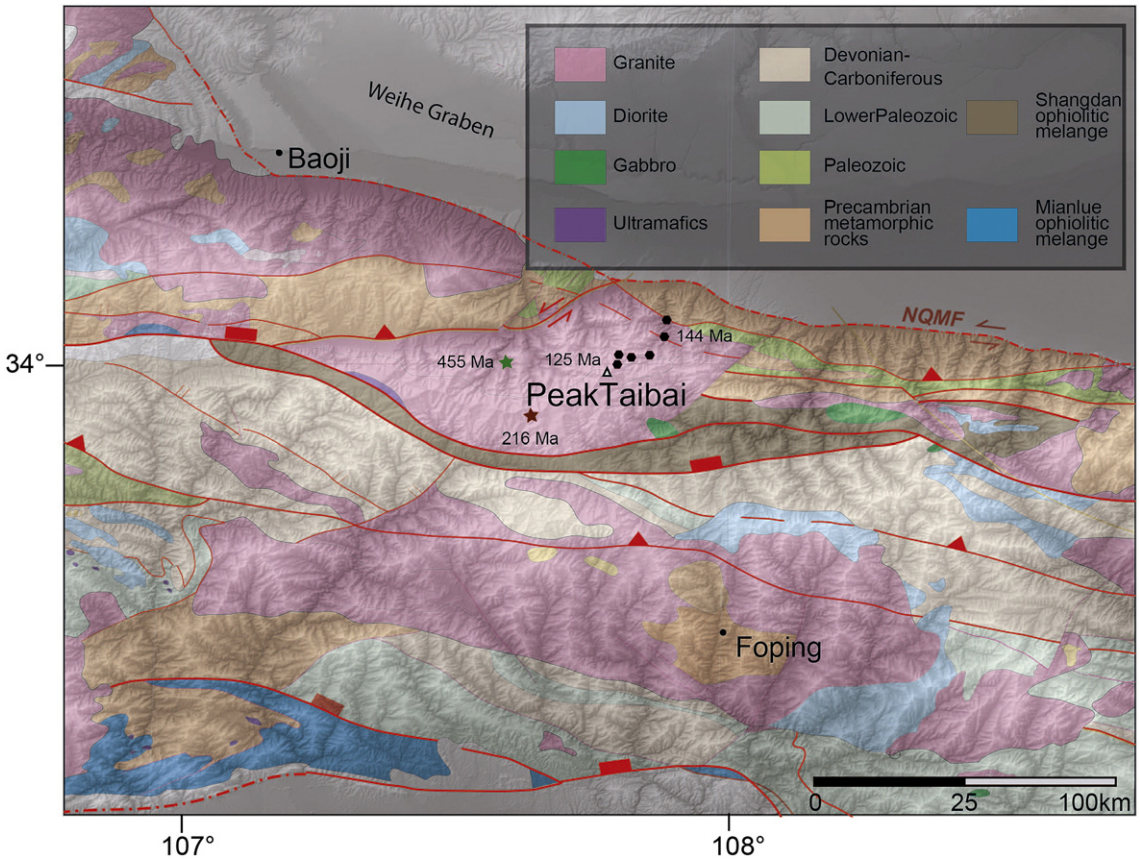

Fig. 2. Digital elevation model with superimposed geological map of the Taibai region, Qinling Mountains modified after Liu et al. (1996). Sample locations along the Taibai profile are indicated. New U–Pb data for the composite Taibai granite from this study are indicated in black, data from the literature are marked with a green (Zhou et al., 1994) and red (Xiao et al., 2000) asterisk. NQMF = North Qinling margin fault.

event (4) with WNW–ESE shortening and surface uplift and exhumation. NE–SW extension (5) was dominant during Late Miocene times. No structural data was found for the latest Miocene–Early Pliocene time (~9–3.5 Ma). A last tectonic phase was defined for Late Pliocene–Quaternary times, when NNW–SSE extension (6) occurred. Interestingly, alkaline volcanics extruded between 23 and 7 Ma in the western Qinling Mountains (Tang et al., 2012). At present, normal movement north of the Qinling Mountains in the NCB contrasts with eastward extrusion of the South China Block at a rate between 5 and 15 mm/a (Mercier et al., 2013; Wang et al., 2001; Zhang et al., 1998).

A number of studies have addressed the cooling history of the Qinling Mts. using low-temperature thermochronology (Chen et al., 2001; Enkelmann et al., 2006; Hu et al., 2006; Yin et al., 2001). Recently, Liu et al. (2013) carried out AFT analyses along a similar vertical profile of the Taibai Mountain but located further to the west. They found an age gradient similar to our results, however, their AFT ages seem to be systematically younger than our AFT, and in parts even younger than our AHe data, a contradiction which cannot be readily dissolved at that stage. They find acceleration in cooling at ca. 10 Ma along the Taibai and the Huashan transects (Fig. 1). A somewhat younger onset of rapid cooling (9–4 Ma) in the southwestern Qinling Mountains was described by Enkelmann et al. (2006). A young (mostly Miocene) exhumation event following a long period of thermal stability is also a common feature of cooling paths compiled for the eastern Tibetan Plateau (Roger et al., 2010, 2011).

3. Materials and methods

We collected seven granite and one amphibolite samples of the Taibai granite along an elevation profile from altitudes 929 to 3375 m. Table 1 gives an overview of all samples, applied methods and results. On one sample (QL-49), hornblende barometry was carried out to reveal the depth of intrusion. Two representative granite samples (QL-44 and QL-47A) were selected for U–Pb zircon dating (Table 2). From

Table 1
Summary of locations, lithologies and results for samples from the Taibai transect.

Lithology	Altitude (m a.s.l.)	Methods applied	U–Pb age ± 1σ	Ar–Ar age ± 1σ (amph)	Ar–Ar age ± 1σ (bt)	Ar–Ar age ± 1σ (Kf)	AFT age ± 1σ	AHe age ± 1σ
Granite	3375	U–Pb; Ar–Ar (Kf, bt), AFT	124.4 ± 1.3		120.0 ± 0.6	117.0 ± 1.4	67.1 ± 2.7	
Bt-amphibolite	3375	Ar–Ar (bt, amph)		122.2 ± 0.7	123.4 ± 0.3			
Granite	3261	AHe						44.9 ± 2.8
Granite	2755	AHe; AFT					58.3 ± 3.3	35.5 ± 1.1
Granite	2196	Ar–Ar (Kf, Bt); AFT; AHe			116.9 ± 1.0	113.0 ± 0.3	49.3 ± 2.5	26.7 ± 1.3
Granite	1750	p–T; Ar–Ar (bt); AFT; AHe			115.0 ± 0.4		40.3 ± 2.9	22.5 ± 3.6
Granite	1163	U–Pb; Ar–Ar (Kf, Bt); AFT; AHe	155.5 ± 3.4		119.9 ± 0.7	111.1 ± 1.9	34.5 ± 1.8	21.3 ± 1.9
Granite	929	AFT; AHe					26.6 ± 2.0	13.6 ± 0.9

Table 2
U–Pb analytical data of samples QL-44 and QL-47A of the Taibai granite.

Sample spot #	Isotope ratios								Ages								Concordia
	$^{207}Pb/^{206}Pb$	1σ	$^{207}Pb/^{235}U$	1σ	$^{206}Pb/^{238}U$	1σ	$^{208}Pb/^{232}Th$	1σ	$^{207}Pb/^{206}Pb$	1σ	$^{207}Pb/^{235}U$	1σ	$^{206}Pb/^{238}U$	1σ	$^{208}Pb/^{232}Th$	1σ	
QL-44-01	0.0470	0.0015	0.1566	0.0033	0.0240	0.0004	0.0072	0.0001	49.8	75.1	147.7	2.9	152.8	2.3	144.5	2.0	96.7
QL-44-02	0.0457	0.0014	0.1594	0.0029	0.0252	0.0004	0.0071	0.0001	0.1	51.2	150.2	2.6	160.1	2.4	142.1	2.0	93.8
QL-44-03	0.0460	0.0016	0.1564	0.0039	0.0245	0.0004	0.0070	0.0001	0.1	77.6	147.6	3.4	156.2	2.4	141.7	2.9	94.5
QL-44-04	0.0473	0.0016	0.1717	0.0037	0.0262	0.0004	0.0079	0.0001	65.0	76.8	160.8	3.2	166.4	2.5	159.5	2.5	96.6
QL-44-05	0.0474	0.0015	0.1572	0.0033	0.0239	0.0004	0.0063	0.0001	66.6	75.3	148.3	2.9	152.5	2.3	126.6	1.8	97.2
QL-44-06	0.0508	0.0016	0.1711	0.0035	0.0243	0.0004	0.0073	0.0001	233.0	72.0	160.3	3.0	154.6	2.3	146.6	2.3	103.7
QL-44-07	0.0539	0.0020	0.1987	0.0053	0.0266	0.0004	0.0074	0.0001	367.9	80.4	184	4.5	169.1	2.6	147.9	2.8	108.8
QL-44-08	0.0480	0.0015	0.1525	0.0027	0.0230	0.0003	0.0070	0.0001	95.9	71.8	144.1	2.4	146.3	2.2	140.9	2.0	98.5
QL-44-09	0.0476	0.0015	0.1599	0.0033	0.0243	0.0004	0.0083	0.0001	77.6	75.5	150.6	2.9	154.5	2.3	166.7	2.8	97.5
QL-44-10	0.0476	0.0015	0.1637	0.0033	0.0248	0.0004	0.0082	0.0001	79.1	75.4	153.9	2.9	158	2.4	164.7	2.2	97.4
QL-44-11	0.0488	0.0016	0.1679	0.0036	0.0249	0.0004	0.0077	0.0001	137.7	76.4	157.6	3.2	158.4	2.4	155.3	2.5	99.5
QL-44-12	0.0482	0.0016	0.1661	0.0035	0.0249	0.0004	0.0083	0.0001	107.9	75.9	156	3.0	158.7	2.4	166.7	2.9	98.3
QL-44-13	0.0500	0.0017	0.1692	0.0040	0.0245	0.0004	0.0081	0.0001	195.6	79.0	158.7	3.5	155.7	2.4	162.9	2.9	101.9
QL-44-14	0.0529	0.0017	0.1776	0.0035	0.0243	0.0004	0.0073	0.0001	324.4	71.6	166	3.0	154.6	2.3	147.2	2.2	107.4
QL-44-15	0.0486	0.0044	0.1149	0.0098	0.0171	0.0003	0.0097	0.0003	126.9	198.7	110.4	8.9	109.4	2.2	194.2	6.9	100.9
QL-44-16	0.0528	0.0018	0.1735	0.0037	0.0238	0.0004	0.0087	0.0002	318.4	73.9	162.5	3.2	151.6	2.3	175.1	3.1	107.2
QL-44-17	0.0528	0.0017	0.2316	0.0044	0.0317	0.0005	0.0119	0.0002	321.7	71.2	211.5	3.6	201.3	3.0	239	3.9	105.1
QL-44-18	0.0794	0.0026	0.8925	0.0185	0.0813	0.0013	0.0617	0.0012	1182.6	64.2	647.7	9.9	504.1	7.6	1209.9	22.6	128.5
QL-44-19	0.0499	0.0020	0.1620	0.0049	0.0235	0.0004	0.0064	0.0002	191.4	90.4	152.5	4.3	149.7	2.4	127.9	3.2	101.9
QL-44-20	0.0618	0.0026	0.2419	0.0081	0.0283	0.0005	0.0131	0.0003	668.7	88.8	219.9	6.6	180	2.9	263	6.7	122.2
QL-44-21	0.0535	0.0019	0.1833	0.0041	0.0248	0.0004	0.0098	0.0002	350.4	76.1	170.9	3.5	158.1	2.4	197.3	3.4	108.1
QL-44-22	0.1286	0.0040	5.1089	0.0830	0.2880	0.0044	0.1054	0.0018	2078.7	53.4	1837.6	13.8	1631.4	22.0	2024.8	33.7	112.6
QL-44-23	0.0541	0.0019	0.2054	0.0046	0.0275	0.0004	0.0099	0.0002	374.4	76.2	189.7	3.9	175.1	2.7	199.2	3.5	108.3
QL-44-24	0.0554	0.0019	0.1897	0.0041	0.0249	0.0004	0.0096	0.0002	426.6	74.7	176.4	3.5	158.2	2.4	192.2	3.5	111.5
QL-44-25	0.0500	0.0019	0.1657	0.0043	0.0240	0.0004	0.0104	0.0003	194.9	84.7	155.7	3.8	153.1	2.4	209.1	6.5	101.7
QL-44-26	0.0533	0.0019	0.1843	0.0041	0.0251	0.0004	0.0098	0.0002	340.8	76.7	171.8	3.5	159.8	2.4	196.9	3.6	107.5
QL-44-27	0.0556	0.0018	0.2733	0.0052	0.0357	0.0006	0.0128	0.0003	435.4	71.7	245.3	4.2	225.9	3.4	257.1	5.0	108.6
QL-44-28	0.0521	0.0020	0.1870	0.0052	0.0261	0.0004	0.0099	0.0002	288.2	86.3	174	4.4	165.8	2.6	198.1	4.5	104.9
QL-44-29	0.0544	0.0018	0.1898	0.0037	0.0253	0.0004	0.0110	0.0002	389.2	72.5	176.4	3.2	161.1	2.4	220.9	4.3	109.5
QL-44-30	0.0535	0.0019	0.1806	0.0040	0.0245	0.0004	0.0107	0.0002	351.0	77.0	168.6	3.4	156	2.4	215.2	4.1	108.1
QL-47A-01	0.0476	0.0014	0.1319	0.0020	0.0201	0.0003	0.0065	0.0001	80.7	69.0	125.8	1.8	128	1.9	130.8	1.8	98.3
QL-47A-02	0.0508	0.0015	0.1400	0.0021	0.0200	0.0003	0.0064	0.0001	232.1	66.6	133	1.9	127.5	1.9	129.1	1.8	104.3
QL-47A-03	0.0599	0.0018	0.1531	0.0023	0.0185	0.0003	0.0068	0.0001	600.1	62.3	144.6	2.0	118.3	1.8	137.5	1.9	122.2
QL-47A-04	0.0615	0.0018	0.1633	0.0026	0.0192	0.0003	0.0075	0.0001	658.1	62.6	153.6	2.2	122.8	1.8	151.9	2.1	125.1
QL-47A-05	0.0538	0.0016	0.1438	0.0022	0.0194	0.0003	0.0069	0.0001	360.3	65.6	136.4	2.0	123.8	1.8	138.8	1.9	110.2
QL-47A-06	0.0558	0.0017	0.4818	0.0076	0.0625	0.0009	0.0184	0.0003	445.8	65.0	399.3	5.2	391	5.7	369.3	5.2	102.1
QL-47A-07	0.0498	0.0015	0.1303	0.0020	0.0190	0.0003	0.0066	0.0001	184.7	67.9	124.4	1.8	121.2	1.8	133.8	1.9	102.6
QL-47A-08	0.0577	0.0017	0.1314	0.0021	0.0165	0.0003	0.0076	0.0001	518.3	64.6	125.3	1.9	105.5	1.6	152.9	2.2	118.8
QL-47A-09	0.0488	0.0015	0.1332	0.0021	0.0198	0.0003	0.0066	0.0001	139.8	68.7	127	1.9	126.3	1.9	132.9	1.9	100.6
QL-47A-10	0.0511	0.0015	0.1339	0.0020	0.0190	0.0003	0.0064	0.0001	243.6	66.8	127.6	1.8	121.4	1.8	129.6	1.8	105.1
QL-47A-11	0.0617	0.0019	0.1668	0.0027	0.0196	0.0003	0.0075	0.0001	662.6	63.2	156.6	2.3	125.2	1.9	150.9	2.2	125.1
QL-47A-12	0.0497	0.0015	0.1380	0.0022	0.0201	0.0003	0.0068	0.0001	182.6	68.7	131.2	2.0	128.4	1.9	136.5	2.0	102.2
QL-47A-13	0.0489	0.0015	0.1329	0.0022	0.0197	0.0003	0.0070	0.0001	142.6	70.0	126.7	2.0	125.8	1.9	140.5	2.1	100.7
QL-47A-14	0.0703	0.0021	0.1914	0.0030	0.0198	0.0003	0.0077	0.0001	936.5	60.5	177.8	2.6	126	1.9	155.8	2.2	141.1
QL-47A-15	0.0539	0.0016	0.1395	0.0023	0.0188	0.0003	0.0061	0.0001	367.5	66.9	132.6	2.0	119.8	1.8	122	1.8	110.7
QL-47A-16	0.0513	0.0016	0.1347	0.0022	0.0190	0.0003	0.0068	0.0001	253.9	68.1	128.3	1.9	121.6	1.8	137.2	2.0	105.5
QL-47A-17	0.0494	0.0016	0.1343	0.0024	0.0197	0.0003	0.0076	0.0001	167.3	71.6	128	2.2	125.8	1.9	153.4	2.4	101.7
QL-47A-18	0.0851	0.0026	0.2057	0.0035	0.0175	0.0003	0.0096	0.0002	1317.7	58.9	189.9	3.0	112	1.7	193.2	2.9	169.6
QL-47A-19	0.0491	0.0015	0.1362	0.0024	0.0201	0.0003	0.0079	0.0001	152.5	71.4	129.7	2.1	128.4	2.0	159.9	2.4	101.0
QL-47A-20	0.0520	0.0016	0.1398	0.0023	0.0195	0.0003	0.0068	0.0001	283.3	68.3	132.9	2.1	124.6	1.9	136.3	2.0	106.7
QL-47A-21	0.0527	0.0016	0.1396	0.0022	0.0192	0.0003	0.0067	0.0001	315.0	67.3	132.7	2.0	122.7	1.9	134	2.0	108.1
QL-47A-22	0.0531	0.0016	0.1388	0.0023	0.0190	0.0003	0.0074	0.0001	331.2	68.9	132	2.1	121.1	1.9	148.5	2.2	109.0
QL-47A-23	0.0495	0.0015	0.1306	0.0021	0.0191	0.0003	0.0061	0.0001	169.7	70.0	124.6	1.9	122.2	1.9	121.9	1.8	102.0
QL-47A-24	0.0699	0.0022	0.1629	0.0027	0.0169	0.0003	0.0073	0.0001	924.3	62.2	153.2	2.4	108.1	1.7	146.1	2.2	141.7
QL-47A-25	0.0519	0.0016	0.1392	0.0022	0.0195	0.0003	0.0067	0.0001	280.0	67.9	132.3	2.0	124.2	1.9	135.7	2.0	106.5
QL-47A-26	0.0519	0.0016	0.1390	0.0023	0.0194	0.0003	0.0062	0.0001	280.0	68.7	132.1	2.0	124	1.9	125.2	1.9	106.5
QL-47A-27	0.0518	0.0016	0.1421	0.0023	0.0199	0.0003	0.0067	0.0001	275.7	68.6	134.9	2.1	127	1.9	133.9	2.0	106.2
QL-47A-28	0.0528	0.0016	0.1375	0.0022	0.0189	0.0003	0.0065	0.0001	318.8	68.0	130.8	2.0	120.7	1.9	131.2	2.0	108.4
QL-47A-29	0.0880	0.0027	0.2757	0.0045	0.0227	0.0004	0.0126	0.0002	1383.0	57.7	247.3	3.6	144.8	2.2	252.4	3.8	170.8

ten samples mineral concentrates of amphibole, biotite and K-feldspar have been dated with $^{40}Ar/^{39}Ar$ in order to reveal the cooling history after intrusion. AFT and AHe analyses served to document the low-temperature cooling history of the Taibai massif. We adopted the following closure temperatures (T_c): amphibole 550 ± 25 °C (Harrison, 1981), biotite 300 ± 25 °C (Harrison et al., 1985); K-feldspar 200 ± 25 °C (Lovera et al., 1989), AFT partial annealing zone (APAZ) 60–120 °C (Fitzgerald et al., 1991) and AHe partial retention zone (PAZ) 40–80 °C (House et al., 1999). $^{40}Ar/^{39}Ar$ ages are given at the 1σ, U–Pb, (U–Th–Sm)/He and AFT ages at the 2σ level.

4. Results

In the following we give an overview of all results. More information on analytical procedures and detailed results are given in the e-component.

4.1. P–T estimate

Applying the hornblende barometry (Schmidt (1992) in the modification of Anderson and Smith (1995)) for sample QL-49 yields a

pressure of ca. 4.2 ± 0.2 kbar (at T = 775 °C) corresponding to a depth of ca. 12–13 km (Fig. 3). For the temperature estimate, the geothermometer of Holland and Blundy (1994) was applied. The PET software (Dachs, 2004) was used for calculations.

4.2. LA-ICP-MS zircon U–Pb dating

Results of LA-ICP-MS zircon U–Pb dating are given in Table 2 and concordia diagrams are shown in Fig. 4. We use $^{206}Pb/^{238}U$ ages, since they are generally more precise for an age <1000 Ma. Only those ages are used, which are within a concordancy of 90 and 110%. Zircon grains of sample QL-44 from the lower region of the Taibai Mountain yield a crystallization age of 155.5 ± 3.4 Ma. The sample also contains inherited zircon grains with ages of 201.3 ± 3.0 and 225.9 ± 3.4 Ma interpreted to represent Indosinian ages. The uppermost sample QL-47A gives an age of 124.4 ± 1.3 Ma and contains three inherited grains with ages between 148.6 ± 2.2 Ma and 159.9 ± 2.4 Ma likely inherited from the older Taibai granite.

4.3. $^{40}Ar/^{39}Ar$ dating

An overview of all $^{40}Ar/^{39}Ar$ mineral ages is included in Table 1 and Ar release patterns and isochron plots are shown in Fig. 5. Detailed analyses for all minerals are listed in the e-component. Amphiboles of sample QL-47B yield an age of 122.2 ± 0.7 Ma. Biotite ages range between 115.0 ± 0.4 Ma (QL-49) and 123.4 ± 0.3 Ma (QL-47B). Four biotite concentrates yield staircase $^{40}Ar/^{39}Ar$ release patterns in low-temperature steps. These are a result of Ar loss caused by chloritization, as shown by optical microscopy. The exact age of argon loss is insignificant because of low proportions of radiogenic $^{40}Ar^*$. K-feldspar ages range from 111.1 ± 1.9 Ma (QL-44) to 117.0 ± 1.4 Ma (QL-47A). The K-feldspar release patterns do not show a similar argon loss as indicated by the biotite concentrates from the same samples. Consequently, the Ar loss as observed in the biotite release patterns does not indicate a stage of reheating but rather variable access of hydrothermal water, which led to chloritization of biotite (See Fig. 5.)

4.4. Apatite fission-track and (U–Th–Sm)/He analyses

Results of AFT and AHe analyses are given in Tables 3 and 4. Ages of both AFT and AHe thermochronometers vary significantly with elevation and AHe ages are consistently younger than AFT ages (Fig. 6a). As a result of track annealing AFT ages decrease systematically with increasing palaeo-depth. Ages range from 67.1 ± 2.7 at 3375 m to 26.6 ± 2.0 at 929 m. All ages pass the chi^2-test (Galbraith and Laslett, 1993). The number of track lengths was generally very low and only the uppermost oldest sample (QL-47) yielded sufficient lengths for further interpretation (13.48 ± 1.41 μm; n = 80).

Apparent AHe ages decrease as a result of the diffusive loss of ^4He and range from 51.9 ± 7.3 Ma at 3261 m (QL-46) to 13.6 ± 0.9 Ma at 929 m (QL-50).

5. Interpretation of AFT and AHe data and the derivation of the Taibai cooling history

AFT age–elevation profiles with a distinctive age pattern have become a common tool to infer the low-temperature exhumation history (e.g. Fitzgerald et al., 1995; Wagner and Reimer, 1972). Samples from elevation transects record the passage through progressively lower temperatures as the rock column is exhumed towards the surface (Fitzgerald et al., 1995), assuming a vertical particle pathway (e.g. Parrish, 1983) and a steady closure isotherm at constant depth. However, complications may arise from advection of isotherms due to rapid denudation and the deflection of near-surface isotherm due to topography with compressed isotherms beneath valleys and wider-spaced isotherms beneath ridges (Mancktelow and Grasemann, 1997; Stuwe et al., 1994). Threshold values for perturbation of the 110 °C isotherm are exhumation rates ≥0.5 km/Ma, topographic wavelength of ≥10 km and a relief of ≥2 km (Braun, 2002; Mancktelow and Grasemann, 1997;

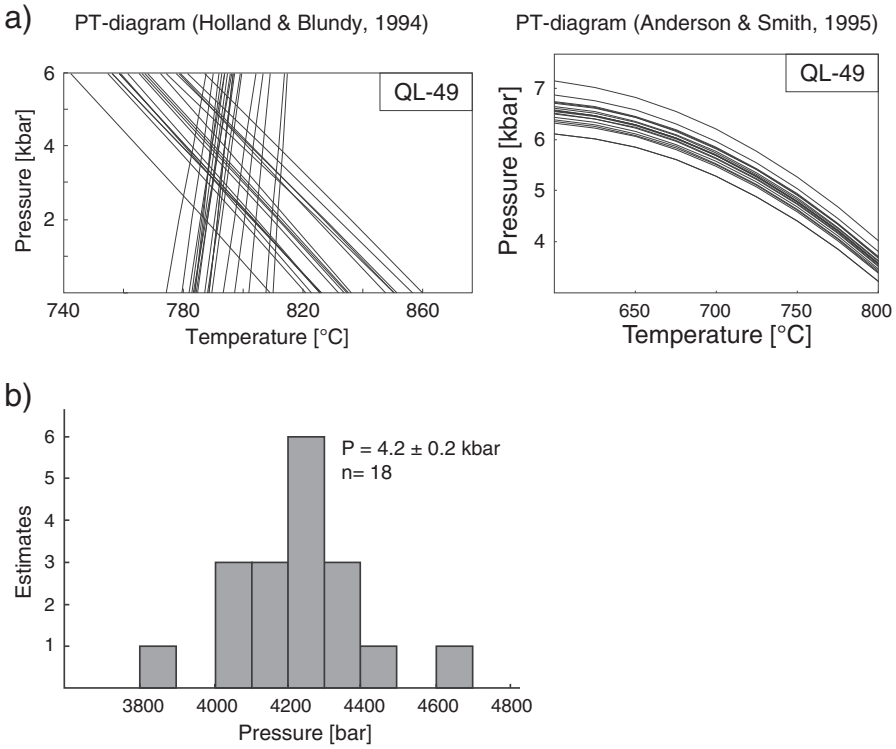

Fig. 3. (a) P–T Estimates for sample QL-49 based on the plagioclase-amphibole thermometer of Holland and Blundy (1994) and Anderson and Smith (1995). (b) Histogram of pressure estimates.

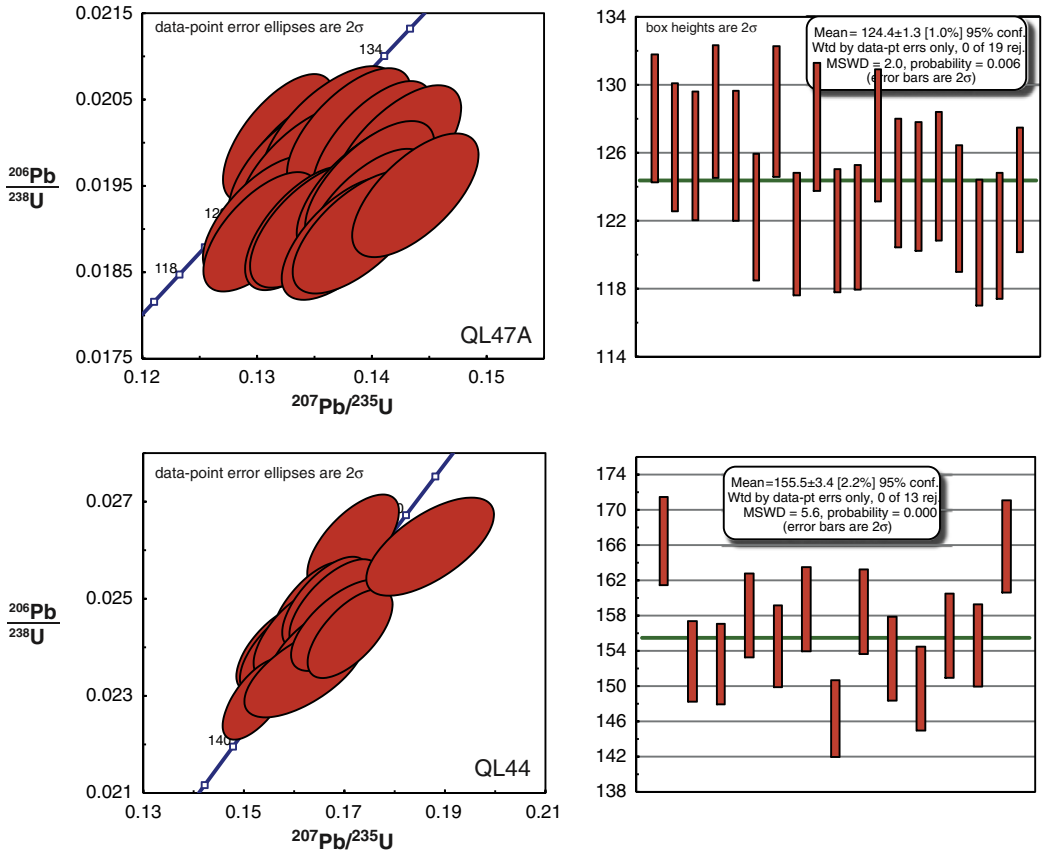

Fig. 4. Concordia diagrams of U–Pb analyses on samples QL-47A and QL-49 with LA-ICP-MS.

Stuwe and Hintermuller, 2000; Stuwe et al., 1994). No topography-induced perturbation of isotherms was found for similar boundary conditions in an AFT study along a tunnel transect (Glotzbach et al., 2009).

The AFT age pattern from the Taibai Mountain shows no discernible deviation from a linear trend, taking the magnitudes of uncertainties into account. However, the simplest possible interpretation of uniform/steady exhumation at an average rate of 0.06 mm/a would yield a much more narrow age range for both thermochronometers and may not account for the observed large age variation. Both the AFT and the AHe data do require a more complex cooling history including a considerable residence time within the APRZ and APAZ, respectively.

Thus, we interpret the age versus elevation/depth profile (Fig. 6a) as uplifted partial annealing and partial retention zones. Fig. 6b shows a concept of expected AFT and AHe ages versus depth profiles within a thermotectonically stable setting: Close to the surface AFT and AHe ages are expected to be constant, indicating an older exhumation event. When entering the PRZ, AHe ages decrease, whereas AFT ages still remain constant. Within the next deeper layer, the apatite partial retention zone (APRZ) and apatite partial annealing zone (APAZ) overlap, and ages of both thermochronometers decrease. When reaching the upper temperature limit of the APRZ, AHe ages will remain constant, whereas AFT ages further decrease until the high-temperature limit of the APAZ is reached. For our data this schematic pattern allows us to derive an estimate of the pre-exhumation palaeo-geothermal gradient (Stockli et al., 2000): Under the assumption that the PRZ ranges from 40 to 80 °C and the PAZ from 60 to 120 °C (dpar values indicate Ca-rich F-apatites, Table 3), the zone of a contemporaneous decrease in ages spans only 20 °C. Following the concept of exhumed AFT-PAZs and AHe-PRZs (Fitzgerald and Gleadow, 1990; Fitzgerald et al., 1995) we interpret the marked inflection point within the AHe profile at ca. 2000 m as the base of the HePRZ and suggest that intensified cooling initiated at around 22–25 Ma. A second inflection point is observed at 1000 m. An apatite PAZ is not well defined, since our AFT data fit well to a linear trend. However, parallel trends of both systems over a vertical distance of more than 1000 m would reduce the geothermal gradient to below 20 °C/km. We therefore propose that the uppermost AFT sample, which shows a slight deviation from a linear trend, was located above the upper (low temperature) limit of the fossil PAZ. By placing the upper PAZ limit at ca. 3000 m and the lower PRZ limit at ca. 2000 m, a palaeo-geothermal gradient in line with a long-term stable situation is derived (see below for a more detailed discussion of the gradient).

In order to derive more robust cooling histories in line with our data from age–elevation-relationships all samples were forward modeled with HeFTy (Ketcham, 2005). Time–temperature histories were derived and the resulting AFT and AHe data were compared with the measured parameters (Fig. 7). As indicated by the goodness-of-fit values (GOF), which range between 0.5 and 1 (Fig. 7), the proposed model successfully integrates our AFT and AHe data sets and provides a coherent interpretation of the measured ages.

Based on the Ar–Ar ages, the AFT and AHe age–elevation profile, and HeFTy modeling, we suggest the following five-step cooling history (Fig. 7): (1) An early Cretaceous exhumation event brought most of our samples into the partial annealing/retention zones. This phase of rapid cooling (ca. 30 °C/Myr) following emplacement of the granite body is constrained by Ar–Ar dating. (2) It was followed by a long period of very slow, continuous cooling (<1 °C/Myr) between ca. 100 and 25 Ma. (3) Intensified cooling (ca. 5 °C/Myr) started at ca. 22–25 Ma (break-in-slope of AHe data). Preceded by (4) a phase of again slow cooling, (5) a last pulse of exhumation and topography building brought the rocks to the surface. By modeling and by comparisons with other low-T studies (see below for discussion) the onset of this youngest phase of minor cooling is bracketed between ca. 7 and 5 Ma.

The final cooling of the lowermost sample differs from the other samples, as indicated by the second break in slope at ca. 1000 m

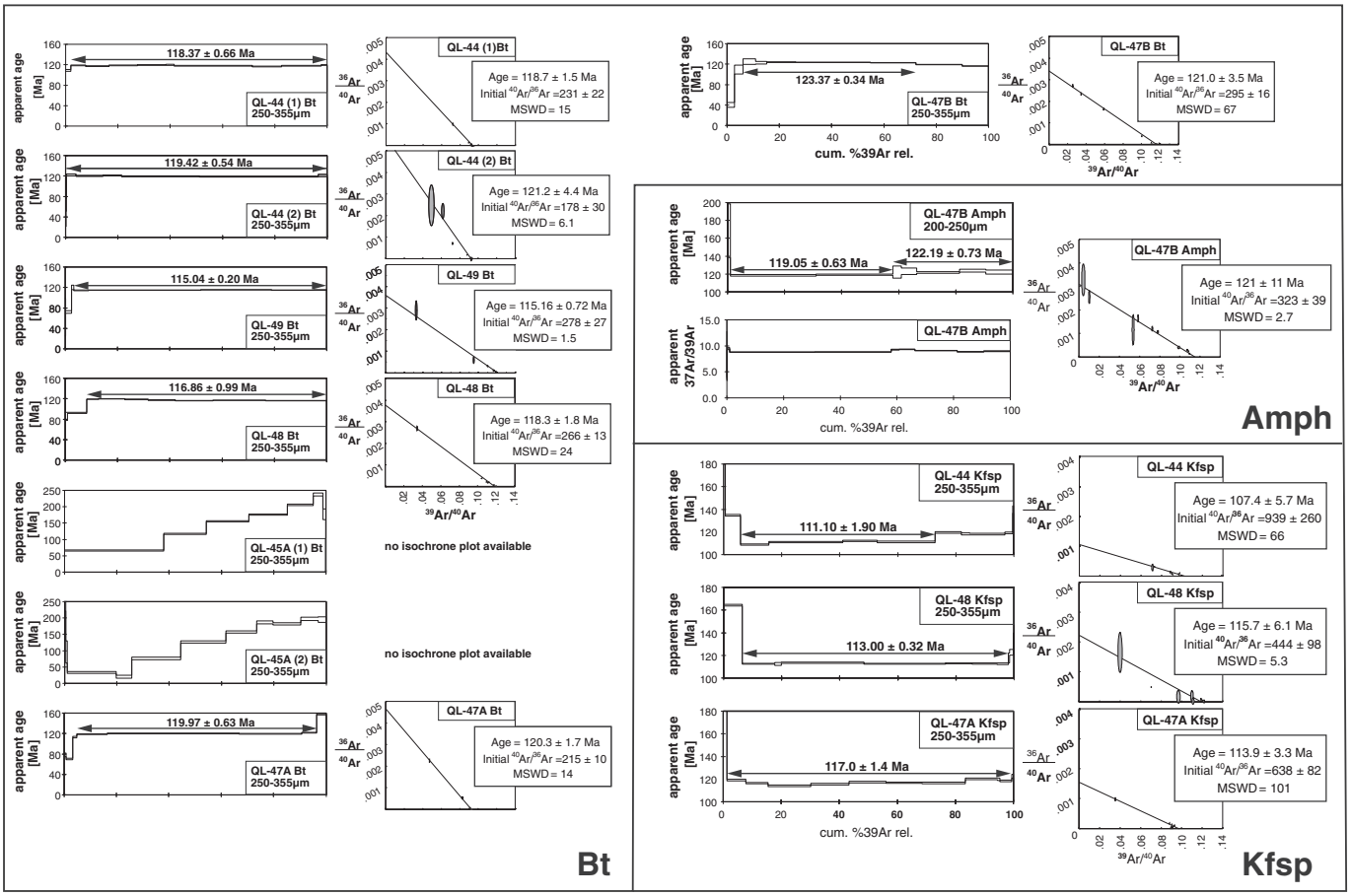

Fig. 5. $^{40}Ar/^{39}Ar$ release patterns of amphibole, biotite and K-feldspar from the samples of the Taibai granite.

(Fig. 6a). For this sample, a reheating event, probably due to hydrothermal fluxes, must have occurred. Such a scenario seems likely, considering, that the sample is situated closest to the range-bounding normal fault. Indeed, numerous hot springs occur along the North Qinling margin fault (e.g. Huaqing). Alteration fabrics visible in thin section, e.g. the transformation of feldspar and biotite, also support this interpretation.

6. Discussion

Two main aspects of the results shall be discussed further: (1) the Late Jurassic to Cretaceous intrusion and high-temperature cooling ages and its implications for Early Cretaceous Yanshanian tectonic models of Central China, and (2) the subsequent, ca. 75 Myr long history of slow cooling followed by episodic cooling and its relation to the India–Asia collision and other major tectonic events.

6.1. Yanshanian magmatism and cooling along a lithospheric-scale tear fault

The Taibai granite experienced multiple intrusion episodes: For its northern unit, Zhou et al. (1994) reported a whole-rock Rb–Sr age of 455 Ma, and Xiao et al. (2000) an age of 216 ± 14 Ma. Our analyses yield two different ages of 155.5 ± 3.4 Ma and 124.4 ± 1.3 Ma, which represent the youngest (known) stages of intrusion activity of this composite pluton (Fig. 2). Since all new $^{40}Ar/^{39}Ar$ mineral ages postdate the younger U–Pb zircon age (124.4 ± 1.3 Ma), samples must have resided at high temperatures or were thermally affected by the youngest intrusion. Upper Jurassic to Cretaceous intrusions are widespread in the North Qinling–Dabie Mts. further east and thus granitoids from the Taibai vertical profile form the westernmost tip of a ca. 1200 km long granitic belt with similar ages (Fig. 1) (Dong et al., 2011; Mao et al., 2005; Ye et al., 2006; Zhu, 1995; Zhu et al., 2008). Several 100s of km to the WNW of Taibai, Li et al. (2013) recently reported alkaline basalt and basaltic andesite with an age of ca. 106–103 Ma which would imply a further extension of the magmatic belt. The linear granite belt includes a wide range of compositions including I-, S- and A-type granites, alkaline rocks and widespread Mo mineralization. Since most bear a calcalkaline signature, they were traditionally interpreted to record southward intracontinental subduction of the North China Block (NCB), accompanied by abundant gold and molybdenite mineralizations (Du et al., 1994; Huang et al., 1994; Li et al., 2003; Stein et al., 1997; Wang et al., 2012). However, up to now a corresponding mantle slab has not been detected, although a number of geophysical transects cross this boundary (Chen et al., 2009; van der Meer et al., 2010). Also, large-scale overthrusts of the Qinling onto the NCB have not been reported. Mao et al. (2010) presented new SHRIMP U–Pb ages from the Eastern Qinling region and differentiated between a Late Jurassic–Early Cretaceous (158 ± 3 to 136 ± 2 Ma) and an Early Cretaceous (134±1 to 108 ± 2 Ma) pulse. They relate both episodes to subduction of the Izanagi plate (ancient Pacific plate) beneath Eastern China, which occurred at a shallow angle during the earlier phase (Li and Li, 2007). However, since this subduction is far away and the orientation of the granite belt is ca. perpendicular to the Pacific coast, it may not explain the entire Late Jurassic–Early Cretaceous-aged granite belt. Based on the mixed nature and the asthenospheric contribution to the melt, we suggest magma uprise along a lithospheric-scale tear fault as a consequence of lithospheric thinning, asthenospheric upwelling and partial melting (Mao et al., 2008, 2011). This would fit into a model recently proposed by Faure et al. (2012), within which west-directed intracontinental subduction of the NCB underneath the Helanshan fold-and-thrust belt plays a key role (Fig. 8a). The N–S trend of the Helanshan contrasts with the predominantly E–W striking tectonic framework of

Table 3
Results from apatite fission-track analysis. n is the number of grains counted. ρ_s, ρ_i, ρ_d and N_s, N_i, N_d are the number and density of spontaneous, induced and dosimeter tracks respectively; χ^2 is the chi-squared probability. A zeta factor of 362.8 ± 3.27 (for Heberer) was based on standard calibrations of Durango and Fish Canyon Tuff using the external detector method and CN5 as the dosimeter glass. All reported ages are central ages. The etched pit parameter Dpar (Donelick, 1993) was measured to constrain annealing kinetics (4 dpars for each grain).

Sample	Altitude (m)	n	$\rho_s \times 10^5$ cm^{-2}	N_s	$\rho_i \times 10^6$ cm^{-2}	N_i	P (χ^2)	$\rho_d \times 10^6$ cm^{-2}	N_d	Age, Ma	±1σ	U (ppm)	Mean Dpar (μm)	SD (μm)	Mean length and Dpar (μm, 1σ)	Number of lengths
QL-50-06	929	20	1.611	200	1.727	2144	67	1.576	4960	26.6	2.0	13.7	1.45	0.17	–	–
QL-44-06	1163	20	3.477	464	2.911	2120	53	1.595	5020	34.5	1.8	22.8	1.65	0.15	13.67 ± 1.71 1.66 ± 0.4	11
QL-49-06	1750	19	1.582	237	1.122	1681	96	1.58	4972	40.3	2.9	8.9	1.7	0.16	–	–
QL-48-06	2196	17	4.789	476	2.778	2761	81	1.584	4984	49.3	2.5	21.9	1.65	0.15	13.03 ± 1.91 1.74 ± 0.2	14
QL-45A-06	2755	15	4.787	405	2.361	1997	79	1.591	5008	58.3	3.3	18.5	1.7	0.16	12.97 ± 2.0 1.93 ± 0.13	22
QL-47A-06	3375	19	7.348	999	3.116	4236	33	1.587	4996	67.1	2.7	24.5	1.96	0.16	13.48 ± 1.41 1.89 ± 0.12	80

China and eastern Asia (Figs. 1 and 8). Crustal-scale shortening within the Helanshan fold-and-thrust belt between the continental NCB in the east and the Alashan Block in the west (Fig. 1) and eastward vergency within the Helanshan and Zhuozi fold-and-thrust belt have been outlined by Darby and Ritts (2002) and corroborate this model. The presence of a foreland basin in front and significant shortening within the Helanshan indicate significant intracontinental convergence between the NCB and the Alashan Block during Late Jurassic and Early Cretaceous (Darby and Ritts, 2002).

As proposed by Faure et al. (2012) the NCB is therefore an isolated indentation-type block. The Yinshan–Yanshan belt represents its northern lateral boundary and the North Qinling–Dabie belt its sinistral transpressive southern transform boundary transferring and connecting westward motion of the NCB against the South China Block (Fig. 8). The driving mechanism could be flat-slab subduction, which leads to increased interplate coupling and transmission of stress and deformation far into the upper plate (e.g. English et al., 2003; Gutscher et al., 2000). Such Late Jurassic to Early Cretaceous flat-slab subduction (Fig. 8b) preceded by slab rollback (Fig. 8c) was recently proposed by Kiminami and Imaoka (2013). The Cretaceous-aged, ca. E- to ESE-trending strike-slip faults and related basins within the Qinling Mountains (Zhang et al., 2001) represent part of a tear fault connecting shortening at the southern tip of the Helanshan with an unknown tip point east of present-day Dabie Shan.

Since reliable markers are missing the amount of indentation of the NCB is unclear. One speculative marker might be the correlation of the Palaeozoic Shangdan suture in the Qinling Mts. with the Palaeozoic North Quaidam suture zone in the southern Qilian Mts. This would yield an offset of 200 to 400 km, which is cumulative for both Cretaceous and Cenozoic times.

Depending on the complex activity along the lithospheric-scale tear fault, some of the granitoids underwent rapid cooling subsequent to intrusion, whereas others resided for a longer time at depth. $^{40}Ar/^{39}Ar$ mineral ages record intense cooling from ca. 550° (amphibole) to 200 °C (K-feldspar) between ca. 123 Ma and 111 Ma (Fig. 7). A phase of strong surface uplift and denudation is corroborated by the presence of ca. E-trending ductile shear zones throughout the Qinling Mts., which yield similar Late Jurassic to Early Cretaceous mineral ages for shearing, and which are connected with narrow, fault-bounded Lower Cretaceous sedimentary basins filled with conglomerates and sandstones. Along the southern margin of the Qinling Mts., Lower Jurassic strata were overthrusted, and the foreland fold–thrust belt also implies the growth of topography (Ratschbacher et al., 2003; Zhang et al., 2001). Evidence for Late Jurassic to Cretaceous rapid exhumation of some sectors of the Qinling orogen and adjacent areas was also found in other thermochronological studies (Chang et al., 2010; Hu et al., 2006; Ratschbacher et al., 2006; Shen et al., 2007; Zheng et al., 2004).

Deformation and magmatic activity concentrated along the 1200 km long E–W belts might further be a consequence of large and sharp steps in lithospheric thickness, defining long-lasting zones of weakness between the Ordos Block and the adjacent Qinling–Dabie and Yinshan–Yanshan orogens (Chen et al., 2009). Upwelling magma was possibly deflected around the deep lithospheric root of the Ordos Block, causing widespread late Mesozoic igneous rocks around but much weaker magmatic activity within the Ordos basin (e.g. Yuan et al., 2007).

In our model the Helanshan fold–thrust belt represents an intracontinental suture. Based on global mantle tomography van der Meer et al. (2010) outline a remnant of a subducted oceanic plate beneath Central China (Central China slab). Slab ages are given as 260/250 to 121–84 Ma, bracketing the onset and end of subduction. Van der Meer et al. (2010) interpret the Central China slab as the remnant of eastward subducted Palaeotethys lithosphere below Cathaysia and as the southern continuation of the Mongol–Okhotsk slab. We suggest that the intracontinental subduction proposed by Faure et al. (2012) is linked to a larger, segmented, possibly mixed oceanic/continental subduction zone, traced by the today's N–S trending Central China slab deeply

Table 4
Results from apatite (U–Th–Sm)/He analysis. Amount of helium is given in nano-cubic-cm in standard temperature and pressure. Amount of radioactive elements are given in nanograms. Ejection correct. (Ft): correction factor for alpha-ejection (according to Farley et al., 1996; Hourigan et al., 2005). Uncertainties of helium and the radioactive element contents are given as 1 sigma, in relative error %. Uncertainty of the sample average age is 1 standard error, as (SD) / (n)1/2; where SD = standard deviation of the age replicates and n = number of age determinations. Division of standard deviation is applied only in cases of n > 2.

Aliquot	He		^{238}U			^{232}Th			Th/U ratio	Sm			Ejection	Uncorr.	Ft-corr.	1σ	Sample unweighted aver. & s.e.	
	Vol.	s.e.	Mass	s.e.	Conc.	Mass	s.e.	Conc.		Mass	s.e.	Conc.	correct.	He-age	He-age			
	[ncc]	[ncc]	[ng]	[ng]	[ppm]	[ng]	[ng]	[ppm]		[ng]	[ng]	[ppm]	(Ft)	[Ma]	[Ma]	[Ma]		
QL-44 a2	0.350	0.007	0.111	0.002	12.1	0.096	0.002	10.5	0.87	1.388	0.048	150	0.80	19.9	24.9	0.6		
QL-44 a3	0.166	0.003	0.081	0.002	16.2	0.037	0.001	7.3	0.45	0.666	0.024	132	0.71	14.4	20.3	0.5		
QL-44 a4	0.215	0.004	0.110	0.002	16.3	0.052	0.001	7.7	0.47	0.898	0.031	133	0.74	13.7	18.6	0.5	21.3	1.9
QL-50 a1	0.036	0.001	0.020	0.001	3.6	0.016	0.000	2.9	0.81	0.378	0.013	70	0.77	11.1	14.5	0.6		
QL-50 a2	0.098	0.002	0.058	0.001	6.0	0.036	0.001	3.8	0.63	0.828	0.038	86	0.87	11.1	12.7	0.4	13.6	0.9
QL-46 a1	0.696	0.012	0.145	0.003	18.4	0.023	0.001	2.9	0.16	1.728	0.060	218	0.72	34.9	48.4	1.1		
QL-46 a2	0.595	0.011	0.131	0.002	12.6	0.025	0.001	2.4	0.19	1.825	0.063	175	0.78	32.3	41.5	1.0	44.9	2.8
QL-48 a1	0.170	0.004	0.055	0.001	8.9	0.036	0.001	5.8	0.65	0.747	0.026	122	0.76	20.3	26.7	0.7		
QL-48 a2	0.111	0.003	0.044	0.001	9.8	0.022	0.001	4.8	0.49	0.537	0.020	120	0.71	17.2	24.4	0.7		
QL-48 a3	0.438	0.008	0.127	0.002	9.6	0.089	0.002	6.7	0.70	1.398	0.049	105	0.79	22.7	28.9	0.7	26.7	1.3
QL-45 a1	0.107	0.002	0.029	0.001	10.5	0.018	0.001	6.7	0.64	0.251	0.009	91	0.70	24.9	35.5	1.1		
QL-49 a1	0.053	0.002	0.019	0.001	7.0	0.011	0.000	3.8	0.55	0.367	0.014	132	0.69	17.7	25.6	1.0		
QL-49 a2	0.022	0.001	0.014	0.001	6.0	0.007	0.000	3.2	0.53	0.311	0.011	136	0.65	10.0	15.3	0.8		
QL-49 a3	0.061	0.002	0.019	0.001	5.4	0.011	0.000	3.2	0.60	0.464	0.017	131	0.74	19.8	26.6	1.0	22.5	3.6

buried in the mantle (van der Meer et al., 2010). In such a case, the orientation of the slab is now different from the mostly ca. W–E trending subduction zones proposed for Eastern Asia (Yin and Harrison, 2000). The Banda arc may represent an appropriate model for the interaction of oceanic and continental lithosphere and rotation of subducted slabs (Spakman and Hall, 2010).

Our model shows similarities to the classical STEP fault model of Govers and Wortel (2005), in which a STEP fault is defined as the lateral boundary of a retreating subduction zone. However, in our case the fault is propagating away from the intracontinental subduction zone as a lateral transform boundary of an indenting continental block (Fig. 8a).

6.2. The Cenozoic cooling history of the Taibai granite

After the initial stage of rapid cooling (cooling phase 1 in Fig. 7), a stable thermotectonic environment developed and prevailed for ca. 75 Myr (cooling phase 2). During this phase of insignificant exhumation and peneplanation the age patterns and the distinctly shaped APAZ and APRZ evolved (Fig. 6a). Based on these patterns we derived a geothermal gradient of ca. 20 °C/km. Such a pre-exhumation thermal structure seems reasonable for a thickened, stable crust within a plate interior setting. Widespread Mesozoic lithospheric extension (decratonization) with high heat flow and voluminous magmatism was restricted to the eastern part of the NCB (Chen et al., 2009; Zhang, 2013), and even beneath the younger rift systems surrounding the Ordos basin the crust is relatively thick (>37 km) (Li et al., 2006; Zheng et al., 2006). An identical gradient of 20 °C/km was suggested for the Mesozoic for the Sichuan basin by Richardson et al. (2008).

Based on our AHe profile we find a further pronounced cooling phase (cooling phase 3) for the latest Oligocene. However, this cooling phase did not bring our samples to the surface, and our data clearly argue for pulsed exhumation since the latest Oligocene (see below for discussion of latest cooling stage). Intensified cooling during ca. 22–25 Ma is corroborated by palaeostress analyses from Mercier et al. (2013) for the Weihe graben. They describe the Late Oligocene–Early Miocene as a period of major transpression, uplift and exhumation. Sediment accumulation rates in the graben show a marked increase at ca. 25 Ma (inset Fig. 7). Thus the sedimentological record, stored in the adjacent basin supports that denudation and surface uplift of the range accompanied rapid cooling. A slightly younger (~21 Ma) onset of rapid cooling and denudation were found for the Ordos Basin, based on a compilation of FT ages and the sedimentary history of the basin and the surrounding grabens (Yuan et al., 2007). Intensified thermotectonism was widespread during this phase, e.g. major fault reactivation occurred in the Himalayas (e.g. Le Fort, 1975), as well as major compression in the Northern Tibetan Plateau (Jolivet et al., 2001). Whether major plate boundary reorganizations in the Pacific were the underlying cause for intensified thermotectonism or if these observations are at all related to the same process remains a matter of debate (for more details see Mercier et al., 2013).

So far, the long-term cooling history derived from the Taibai vertical transect is rather similar to cooling paths from a wide area ranging from eastern Tibet to the Dabie Shan: Roger et al. (2011) compiled t–T-paths from the eastern part of the Tibetan Plateau and find a long period of at least 100 Myr without major tectonic events, erosion or sedimentation following initial rapid cooling for the South Songpan–Garzê, Kunlun and Yidun Blocks. This phase of tectonic quiescence was superseded by exhumation linked to the uplift of the Tibetan Plateau starting at ca. 30 Ma. Based on low-T thermochronology from samples from the Sichuan basin Richardson et al. (2008) found evidence for widespread erosion of 1–4 km that began sometime after 40 Ma. They correlate this event with the reorganization of the drainage pattern and the transition from internal to external drainage, which, according to Roger et al. (2011) might also indicate the onset of topography building in NE Tibet. In a recent contribution, Shi et al. (2012) derive a strikingly similar long-term cooling pattern for samples from the Dabashan at the interface of

the Sichuan basin and the Qinling–Dabie orogenic belt: AFTA and thermal track length modeling indicate rapid cooling before 130–90 Ma and after 25 Ma and slow cooling in-between.

All these thermochronological studies have in common that no major signal of rapid cooling is preserved for the time of the collision of India with Asia at ca. 50 Ma (e.g. Searle et al., 1987; Tapponnier and Molnar, 1977). However, younger (mostly Miocene) exhumation/cooling events have often been interpreted as far-field effects of this collision (e.g. Enkelmann et al., 2006; Liu et al., 2013). Alternatively, Pacific plate subduction or a combination of both geodynamic mechanisms (e.g. Ma et al., 1982) have been suggested to be the trigger for Late Cenozoic tectonism (Ma et al., 1982, 1984; Yin, 2010). Enkelmann et al. (2006) outlined a corridor of rapid cooling and strong exhumation at the very end of the thermal history for samples from the Southwestern Qinling Mountains. Our study, located just outside this zone of late Cenozoic uplift, strongly corroborates their finding of an eastward decrease of latest-stage exhumation. Whereas these authors find final exhumation of 2–3 km for the SW Qinling, our data clearly suggest less than 1 km for the latest step (step 5 of our cooling model). As mentioned above, our samples must have resided above the PRZ prior to final cooling. Thus they do not define an exact onset of final cooling. Modeling yields similarly good results for 7–5 Ma. A Late Miocene intensified cooling and tectonism is corroborated by several studies: One of the strongest arguments comes from the change of course of the Yellow River. Its current bent-shaped course around the Ordos basin (Fig. 1) initiated during Late Miocene to Early Pliocene times due to the development of a topographic divide, which blocked the river from flowing eastward (Lin et al., 2001). Sedimentological evidence from the Weihe graben east of Xi'an strongly points to a marked change in palaeoenvironmental and climatic conditions in late Miocene times (Kaakinen and Lunkka, 2003). A lack of major changes in the surface gradient within the Bahe Formation (deposited between 11 and 7.3 Ma) indicates that no significant surface uplift of the adjacent Qinling Mts. occurred in this time period. However, the onset of aeolian Red Clay deposition immediately above the Bahe sediments is linked to a major uplift phase of the Tibetan Plateau and the development of the monsoon system in China (Zhisheng et al., 2001). Enkelmann et al. (2006) and Wang et al. (2012) bracketed the onset of this final exhumation event between ca. 9 and 4 Ma and both the lower crustal flow model (Clark and Royden, 2000) and the South China Craton acting as a backstop (Tapponnier et al., 2001) equally well describe diminishing exhumation towards the east along a rheologically weak crustal corridor beneath the Qinling Mts. In sum, all these lines of evidence strongly support a causal relationship of our last cooling step initiated at ca. 7–5 Ma and Tibetan Plateau uplift.

7. Conclusions

1. The Taibai granite body is formed by multiple intrusions. New U–Pb zircon data yield Late Jurassic (156 Ma) and Early Cretaceous ages (124 Ma) at a pressure of 4.2 ± 0.2 kbar (at 775 °C) corresponding to a depth of ca. 12–13 km. The Taibai granite forms the westernmost

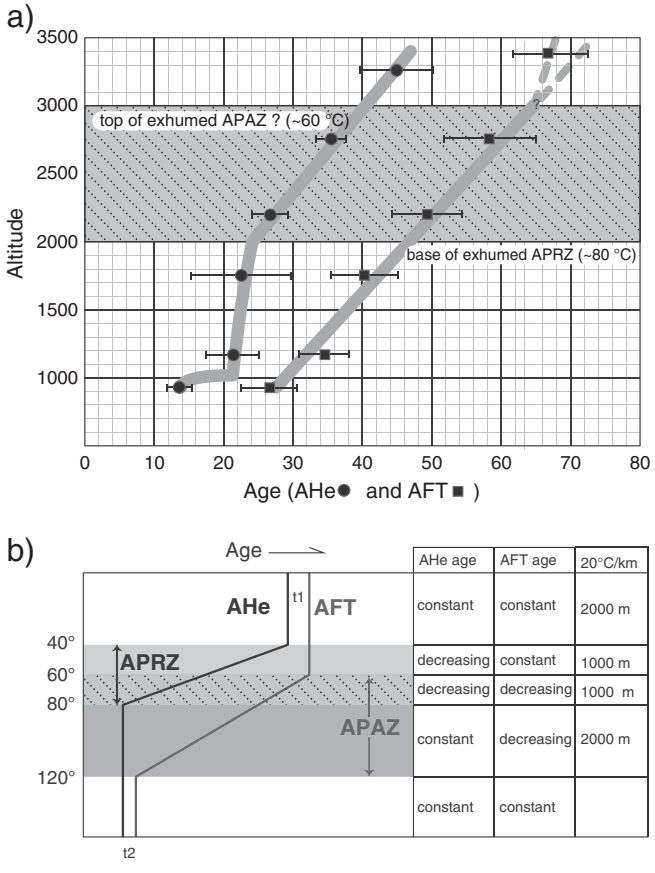

Fig. 6. a) Age-elevation correlation for apatite fission-track and apatite (U–Th–Sm)/He samples from the Taibai mountain. The break-in-slope within the AHe data at ca. 2000 m marks the onset of rapid cooling at ca. 22 to 25 Ma. A second inflection point at ca. 1000 m is interpreted as a later reheating event, probably as a result of hydrothermal fluxes. b) Concept of expected AFT and AHe ages versus depth profiles within a thermotectonically stable setting. Ages of both thermochronometers decrease simultaneously with depth where the APRZ and the APAZ overlap. T_2 marks the onset of an exhumation event, which uplifted the APRZ and APAZ; t_1 marks an older exhumation event.

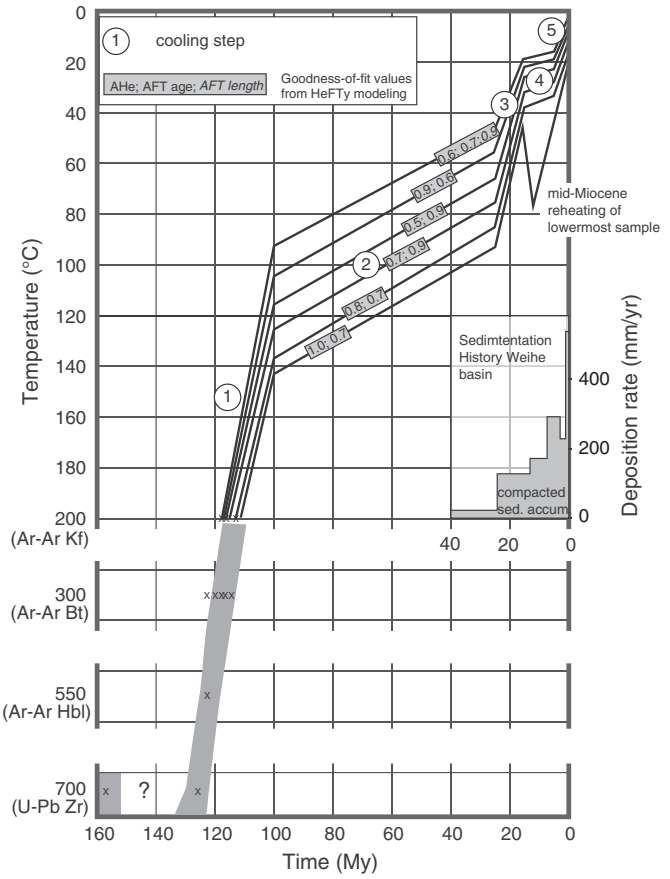

Fig. 7. Cooling history of all samples from the Taibai profile. The cooling paths are constrained by U–Pb ages, Ar–Ar ages, and forward modeling with HeFTy (Ketcham, 2005). Inset shows the sedimentation history of the Weihe graben taken from Liu et al. (2013), modified after Bellier et al. (1988a) and Xing et al. (2005). Note that the Late Oligocene–Miocene onset of intensified cooling is paralleled by an increase in sediment accumulation. Late Miocene cooling also roughly coincides with higher accumulation rates.

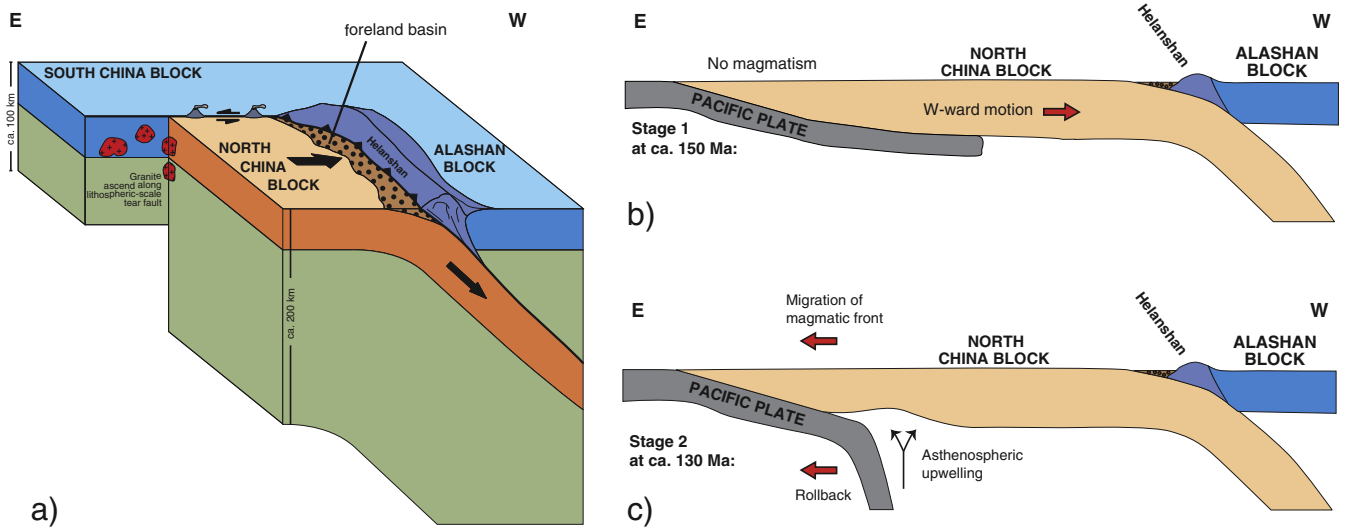

Fig. 8. a) Tectonic model of Yanshanian tectonics according to Faure et al. (2012) and results from this study. b) Schematic cross-sections from the (Palaeo-)Pacific subduction zone in the W to the Alashan Block in the E modified after Kiminami and Imaoka (2013). Flat-slab subduction increases interplate coupling and induces a W-ward motion of the North China Block. c) Slab rollback of the (Palaeo-)Pacific plate prior to flat-slab subduction.

tip of ca. 1200 km long North Qinling–Dabie granite belt at the southern margin of the North China Block.

2. The exhumation history of the Taibai granite is divided into five discrete periods: (1) After emplacement of the youngest intrusions the Taibai samples cooled rapidly at rates of ca. 30 °C/Myr. (2) At ca. 100 Ma cooling rates decreased drastically to less than 1 °C/Myr, and tectonic quiescence prevailed for ca. 75 Ma. (3) A second phase of rapid exhumation was initiated at 22–25 Ma (ca. 5 °C/Myr). (4) Cooling rates decreased at ca. 15 Ma and (5) accelerated again to rates similar to phase 3 during the last ca. 7 Myr.
3. Changes in cooling rate are interpreted as reflecting pulses of tectonic activity. Rapid cooling after emplacement occurred along a large tear fault lateral to the front of a zone of intracontinental convergence. Linking the latest Oligocene–Miocene pulse of deformation and uplift of the Qinling Mountains with the underlying geodynamic causes, e.g. India–Asia collision, Pacific subduction, opening of the Japan Sea is difficult and awaits further detailed studies. Minor late-stage cooling is related to the growth of the Tibetan Plateau and confirms diminishing rates of exhumation eastward.
4. Our study also highlights the usefulness of combining various geochronometric tools to detect the long-term cooling history. In particular, AFT and AHe, which both are most sensitive at shallow crustal levels, applied in tandem along a vertical profile, may delineate episodes of mountain building for areas, where exhumation has not been sufficiently efficient to exhume samples from below the PAZ but from below the PRZ.
5. Finally, the long-term cooling history derived on the Taibai vertical profile underlines, that preexisting weak corridors in the lithosphere are susceptible to deformation and magmatic activity. Located between the rigid Sichuan and Ordos Blocks the Qinling Mts. have been influenced by successive tectonic events, concentrated along major tectonic structures.

Acknowledgments

We acknowledge support of the fieldwork by the Eurasia–Pacific Uninet. We particularly acknowledge support by grant P22110 of the Austrian Science Fund FWF and grants 41190074 and 41225008 of NSFC.

Appendix A. Supplementary data

Supplementary data to this article can be found online at http://dx.doi.org/10.1016/j.tecto.2014.01.011.

References

Anderson, J.L., Smith, D.R., 1995. The effects of temperature and f_{O2} on the Al-in-hornblende barometer. Am. Mineral. 80, 549–559.
Bellier, O., Mercier, J.L., Vergely, P., Long, C.X., Ning, C.Z., 1988a. Cenozoic sedimentary and tectonic evolution of the Weihe graben (Shaanxi Country, Northern China). Bull. Soc. Geol. Fr. 4, 979–994.
Bellier, O., Mercier, J.L., Vergély, P., Long, C.X., Ning, C.Z., 1988b. Evolution sédimentaire et tectonique du graben Cénozoïque de la Wei He (province du Shaanxi, Chine du Nord). Bull. Soc. Geol. Fr. 8, 979–994.
Bellier, O., Vergely, P., Mercier, J.L., Ning, C.Z., Deng, N.G., Yi, M.C., Long, C.X., 1991. Structural and sedimentary analysis in the Li Shan (Mountains) (Shaanxi province, Northern China) — chronology of the extensional tectonic regimes in the Weihe graben. Bull. Soc. Geol. Fr. 162, 101–112.
Braun, J., 2002. Quantifying the effect of recent relief changes on age–elevation relationships. Earth Planet. Sci. Lett. 200, 331–343.
Chang, Y., Xu, C.H., Reiners, P.W., Zhou, Z.Y., 2010. The exhumation evolution of the Micangshan–Hannan uplift since Cretaceous: evidence from apatite (U–Th)/He dating. Chin. J. Geophys. 53, 912–919.
Chen, B.L., Yin, G.M., Li, W.L., Guo, L., Li, L., Lu, Y.C., Guo, S.L., 2001. Determination of tectonic uplift rates of Qinling mountains in central China by fission tracks. Radiat. Meas. 34, 405–408.
Chen, L., Cheng, C., Wei, Z.G., 2009. Seismic evidence for significant lateral variations in lithospheric thickness beneath the central and western North China Craton. Earth Planet. Sci. Lett. 286, 171–183.
Clark, M.K., Royden, L.H., 2000. Topographic ooze: building the eastern margin of Tibet by lower crustal flow. Geology 28, 703–706.
Dachs, E., 2004. PET: petrological elementary tools for Mathematicas: an update. Comput. Geosci. 30, 173–182.
Darby, B.J., Ritts, B.D., 2002. Mesozoic contractional deformation in the middle of the Asian tectonic collage: the intraplate Western Ordos fold–thrust belt, China. Earth Planet. Sci. Lett. 205, 13–24.
Davis, G.A., Zheng, Y.D., Wang, C., Darby, B.J., Zhang, C.H., 2001. Mesozoic tectonic evolution of the Yanshan fold and thrust belt, with emphasis on Hebei and Liaoning provinces, northern China. Paleozoic and Mesozoic Tectonic Evolution of Central Asia: from Continental Assembly to Intracontinental Deformation, 194, pp. 171–197.
Donelick, R.A., 1993. Apatite etching characteristics versus chemical composition. Nuclear Tracks and Radiation Measurements, 21, p. 604.
Dong, S.W., Zhang, Y.Q., Long, C.X., Yang, Z.Y., Ji, Q., Wang, T., Hu, J.M., Chen, X.H., 2008. Jurassic tectonic revolution in China and new interpretation of the "Yanshan Movement". Acta Geol. Sin. 82, 334–347.
Dong, Y.P., Zhang, G.W., Neubauer, F., Liu, X.M., Genser, J., Hauzenberger, C., 2011. Tectonic evolution of the Qinling orogen, China: review and synthesis. J. Asian Earth Sci. 41, 213–237.
Du, A.D., He, H.L., Yin, N.W., Zou, X.Q., Sun, D.Z., Chen, S.Z., Qu, W.J., 1994. A study on the rhenium–osmium geochronometry of molybdenites. Acta Geol. Sin. 68, 339–347.

Engebretson, D.C., Cox, A., Gordon, R.G., 1985. Relative motion between oceanic and continental plates in the Pacific basin. Geol. Soc. Am. Spec. Pap. 206, 1–55.
English, J.M., Johnston, S.T., Wang, K.L., 2003. Thermal modelling of the Laramide orogeny: testing the flat-slab subduction hypothesis. Earth Planet. Sci. Lett. 214, 619–632.
Enkelmann, E., Ratschbacher, L., Jonckheere, R., Nestler, R., Fleischer, M., Gloaguen, R., Hacker, B.R., Zhang, Y.Q., Ma, Y.S., 2006. Cenozoic exhumation and deformation of northeastern Tibet and the Qinling: is Tibetan lower crustal flow diverging around the Sichuan Basin? Geol. Soc. Am. Bull. 118, 651–671.
Farley, K.A., Wolf, R.A., Silver, L.T., 1996. The effects of long alpha-stopping distances on (U–Th)/He ages. Geochim. Cosmochim. Acta 60, 4223–4229.
Faure, M., Lin, W., Chen, Y., 2012. Is the Jurassic (Yanshanian) intraplate tectonics of North China due to westward indentation of the North China block? Terra Nova 24, 456–466.
Fitzgerald, P.G., Gleadow, A.J.W., 1990. New approaches in fission-track geochronology as a tectonic tool — examples from the Transantarctic Mountains. Nucl. Tracks Radiat. Meas. 17, 351–357.
Fitzgerald, P.G., Fryxell, J.E., Wernicke, B.P., 1991. Miocene crustal extension and uplift in southeastern Nevada — constraints from fission-track analysis. Geology 19, 1013–1016.
Fitzgerald, P.G., Sorkhabi, R.B., Redfield, T.F., Stump, E., 1995. Uplift and denudation of the central Alaska Range — a case-study in the use of apatite fission-track thermochronology to determine absolute uplift parameters. J. Geophys. Res. 100, 20175–20191.
Galbraith, R.F., Laslett, G.M., 1993. Statistical-models for mixed fission-track ages. Nuclear Tracks and Radiation Measurements 21, 459–470.
Glotzbach, C., Spiegel, C., Reinecker, J., Rahn, M., Frisch, W., 2009. What perturbs isotherms? An assessment using fission-track thermochronology and thermal modelling along the Gotthard transect. Central Alps Journal of the Geological Society, London, Special Publication, 324, pp. 111–124.
Govers, R., Wortel, M.J.R., 2005. Lithosphere tearing at STEP faults: response to edges of subduction zones. Earth Planet. Sci. Lett. 236, 505–523.
Gutscher, M.A., Spakman, W., Bijwaard, H., Engdahl, E.R., 2000. Geodynamics of flat subduction: seismicity and tomographic constraints from the Andean margin. Tectonics 19, 814–833.
Harrison, T.M., 1981. Diffusion of ^{40}Ar in hornblende. Contrib. Mineral. Petrol. 78, 324–331.
Harrison, T.M., Duncan, I., Mcdougall, I., 1985. Diffusion of ^{40}Ar in biotite — temperature, pressure and compositional effects. Geochim. Cosmochim. Acta 49, 2461–2468.
Holland, T.J.B., Blundy, J., 1994. Non-ideal interactions in calcic amphiboles and their bearing on amphibole-plagioclase thermometry. Contrib. Mineral. Petrol. 116, 433–447.
Hourigan, J.K., Reiners, P.W., Brandon, M.T., 2005. U–Th zonation-dependent alpha-ejection in (U–Th)/He chronometry. Geochim. Cosmochim. Acta 69, 3349–3365.
House, M.A., Farley, K.A., Kohn, B.P., 1999. An empirical test of helium diffusion in apatite: borehole data from the Otway basin, Australia. Earth Planet. Sci. Lett. 170, 463–474.
Hu, S.B., Raza, A., Min, K., Kohn, B.P., Reiners, P.W., Ketcham, R.A., Wang, J.Y., Gleadow, A.J.W., 2006. Late Mesozoic and Cenozoic thermotectonic evolution along a transect from the North China Craton through the Qinling orogen into the Yangtze Craton, central China. Tectonics 25.
Huang, W., Wu, Z.W., 1992. Evolution of the Qinling orogenic belt. Tectonics 11, 371–380.
Huang, D.H., Wu, C.Y., Du, A.D., He, H.L., 1994. Re–Os isotope ages of molybdenum deposits in east Qinling and their significance. Mineral Deposits 13, 221–230.
Jolivet, M., Brunel, M., Seward, D., Xu, Z., Yang, J., Roger, F., Tapponnier, P., Malavieille, J., Arnaud, N., Wu, C., 2001. Mesozoic and Cenozoic tectonics of the northern edge of the Tibetan Plateau: fission-track constraints. Tectonophysics 343, 111–134.
Kaakinen, A., Lunkka, J.P., 2003. Sedimentation of the Late Miocene Bahe Formation and its implications for stable environments adjacent to Qinling Mountains in Shaanxi, China. J. Asian Earth Sci. 22, 67–78.
Ketcham, R.A., 2005. Forward and inverse modeling of low-temperature thermochronometry data. In: Reiners, P., Ehlers, T.A. (Eds.), Low-temperature Thermochronology: Techniques, Interpretations, and Applications, pp. 275–314.
Kiminami, K., Imaoka, T., 2013. Spatiotemporal variations of Jurassic–Cretaceous magmatism in eastern Asia (Tan–Lu Fault to SW Japan): evidence for flat-slab subduction and slab rollback. Terra Nova 25, 414–422.
Le Fort, P., 1975. Himalaya: the collided range. Present knowledge of the continental arc. Am. J. Sci. 275A, 1–44.
Li, Z.X., Li, X.H., 2007. Formation of the 1300-km-wide intracontinental orogen and postorogenic magmatic province in Mesozoic South China: a flat-slab subduction model. Geology 35, 179–182.
Li, S.G., Hart, S.R., Zheng, S.G., Liu, D.L., Zhang, G.W., Guo, A.L., 1989. Timing of collision between the north and south China blocks—the Sm–Nd isotopic age evidence. Sci. China 32, 1393–1400.
Li, X., Yan, W., Li, T., Sun, G., 2001. Analysis on the movement tendency of Xi'an ground fissures. J. Eng. Geol. 9, 39–43 (in Chinese).
Li, Y.F., Mao, J.W., Bai, F.J., Li, J.P., He, Z.J., 2003. Re–Os isotopic dating of molybdenites in the Nannihu molybdenum (tungsten) ore field in the Eastern Qinling and its geological significance. Geol. Rev. 49, 652–659.
Li, S.L., Mooney, W.D., Fan, J.C., 2006. Crustal structure of mainland China from deep seismic sounding data. Tectonophysics 420, 239–252.
Li, Y.-W., Mo, X.-X., Yu, X.-Y., Ding, Y., Huang, X.-F., Wie, P., He, W.-Y., 2013. Geochronological, geochemical and Sr–Nd–Hf isotopic constraints on the origin of the Cretaceous intraplate volcanism in West Qinling, Central China: implications for asthenosphere–lithosphere interaction. Lithos 177, 381–401.
Lin, A.M., Yang, Z.Y., Sun, Z.M., Yang, T.S., 2001. How and when did the Yellow River develop its square bend? Geology 29, 951–954.
Liu, Y., Xu, Z., Shen, X., 1996. Geochemical Map of Qinling Orogenic BeltScience Press, Xi'an.
Liu, J.H., Zhang, P.Z., Lease, R.O., Zheng, D.W., Wan, J.L., Wang, W.T., Zhang, H.P., 2013. Eocene onset and late Miocene acceleration of Cenozoic intracontinental extension in the North Qinling range-Weihe graben: insights from apatite fission track thermochronology. Tectonophysics 584, 281–296.
Lovera, O.M., Richter, F.M., Harrison, T.M., 1989. The ^{40}Ar/^{39}Ar thermochronometry for slowly cooled samples having a distribution of diffusion domain sizes. J. Geophys. Res. 94, 17917–17935.
Ma, X.Y., Deng, Q., Wang, Y.P., Liu, H.F., 1982. Cenozoic graben system in North China. Z. Geomorphol. NF42, 99–116.
Ma, X.G., Liu, G.D., Su, J., 1984. The structure and dynamics of the continental lithosphere in north–northeast China. Ann. Geophys. 2, 611–620.
Mancktelow, N.S., Grasemann, B., 1997. Time-dependent effects of heat advection and topography on cooling histories during erosion. Tectonophysics 270, 167–195.
Mao, J.W., Xie, G.Q., Zhang, Z.H., Li, X.F., Wang, Y.T., Zhang, C.Q., Li, Y.F., 2005. Mesozoic large-scale metallogenic pulses in North China and corresponding geodynamic settings. Acta Petrol. Sin. 21, 169–188.
Mao, J.W., Xie, G.Q., Bierlein, F., Qu, W.J., Du, A.D., Ye, H.S., Pirajno, F., Li, H.M., Guo, B.J., Lie, Y.F., Yang, Z.Q., 2008. Tectonic implications from Re–Os dating of Mesozoic molybdenum deposits in the East Qinling–Dabie orogenic belt. Geochim. Cosmochim. Acta 72, 4607–4626.
Mao, J.W., Xie, G.Q., Pirajno, F., Ye, H.S., Wang, Y.B., Li, Y.F., Xiang, J.F., Zhao, H.J., 2010. Late Jurassic–Early Cretaceous granitoid magmatism in Eastern Qinling, central-eastern China: SHRIMP zircon U–Pb ages and tectonic implications. Aust. J. Earth Sci. 57, 51–78.
Mao, J.W., Pirajno, F., Xiang, J.F., Gao, J.J., Ye, H.S., Li, Y.F., Guo, B.J., 2011. Mesozoic molybdenum deposits in the east Qinling–Dabie orogenic belt: characteristics and tectonic settings. Ore Geol. Rev. 43, 264–293.
Mattauer, M., Matte, P., Malavieille, J., Tapponnier, P., Maluski, H., Xu, Z.Q., Lu, Y.L., Tang, Y.Q., 1985. Tectonics of the Qinling Belt — buildup and evolution of Eastern Asia. Nature 317, 496–500.
Mercier, J.L., Vergely, P., Zhang, Y.Q., Hou, M.J., Belliér, O., Wang, Y.M., 2013. Structural records of the Late Cretaceous–Cenozoic extension in Eastern China and the kinematics of the Southern Tan–Lu and Qinling Fault Zone (Anhui and Shaanxi provinces, PR China). Tectonophysics 582, 50–75.
Molnar, P., Tapponnier, P., 1977. Collision between India and Eurasia. Sci. Am. 236, 30–41.
Parrish, R.R., 1983. Cenozoic thermal evolution and tectonics of the coast mountains of British-Columbia. 1. Fission-track dating, apparent uplift rates, and patterns of uplift. Tectonics 2, 601–631.
Ratschbacher, L., Hacker, B.R., Calvert, A., Webb, L.E., Grimmer, J.C., McWilliams, M.O., Ireland, T., Dong, S.W., Hu, J.M., 2003. Tectonics of the Qinling (Central China): tectonostratigraphy, geochronology, and deformation history. Tectonophysics 366, 1–53.
Ratschbacher, L., Franz, L., Enkelmann, E., Jonckheere, R., Porschke, A., Hacker, B.R., Dong, S.W., Zhang, Y.Q., 2006. The Sino-Korean–Yangtze suture, the Huwan detachment, and the Paleozoic–Tertiary exhumation of (ultra) high-pressure rocks along the Tongbai–Xinxian–Dabie Mountains. Geol. Soc. Am. Spec. Pap. 403, 45–75.
Richardson, N.J., Densmore, A.L., Seward, D., Fowler, A., Wipf, M., Ellis, M.A., Yong, L., Zhang, Y., 2008. Extraordinary denudation in the Sichuan Basin: insights from low-temperature thermochronology adjacent to the eastern margin of the Tibetan Plateau. J. Geophys. Res. 113.
Roger, F., Jolivet, M., Malavieille, J., 2010. The tectonic evolution of the Songpan–Garze (North Tibet) and adjacent areas from Proterozoic to Present: a synthesis. J. Asian Earth Sci. 39, 254–269.
Roger, F., Jolivet, M., Cattin, R., Malavieille, J., 2011. Mesozoic–Cenozoic tectonothermal evolution of the eastern part of the Tibetan Plateau (Songpan–Garzeˆ, Longmen Shan area): insights from thermochronological data and simple thermal modelling. In: Gloaguen, R., Ratschbacher, L. (Eds.), Geological Society of London, Special Publication, London, pp. 9–25.
Schmidt, M.W., 1992. Amphibole composition in tonalite as a function of pressure — an experimental calibration of the Al-in-hornblende barometer. Contrib. Mineral. Petrol. 110, 304–310.
Searle, M.P., Windley, B.F., Coward, M.P., Cooper, D.J.W., Rex, A.J., Rex, D., Li, T.D., Xiao, X.C., Jan, M.Q., Thakur, V.C., Kumar, S., 1987. The closing of Tethys and the tectonics of the Himalaya. Geol. Soc. Am. Bull. 98, 678–701.
Shen, C.B., Mei, L.F., Xu, Z.P., Tang, J.G., Tian, P., 2007. Fission track thermochronology evidence for Mesozoic–Cenozoic uplifting of Daba mountain, central China. Acta Petrol. Sin. 23, 2901–2910.
Shi, W., Zhang, Y.Q., Dong, S.W., Hu, J.M., Wiesinger, M., Ratschbacher, L., Jonckheere, R., Li, J.H., Tian, M., Chen, H., Wu, G.L., Ma, L.C., Li, H.L., 2012. Intra-continental Dabashan orocline, southwestern Qinling, Central China. J. Asian Earth Sci. 46, 20–38.
Spakman, W., Hall, R., 2010. Surface deformation and slab–mantle interaction during Banda arc subduction rollback. Nat. Geosci. 3, 562–566.
Stein, H.J., Markey, R.J., Morgan, J.W., Hannah, J.L., Zak, K., Sundblad, K., 1997. Re–Os dating of shear-hosted Au deposits using molybdenite. In: Papunen, H. (Ed.), Mineral Deposits: Research and Exploration — Where Do They Meet?, Rotterdam, pp. 313–317.
Stockli, D.F., Farley, K.A., Dumitru, T.A., 2000. Calibration of the apatite (U–Th)/He thermochronometer on an exhumed fault block, White Mountains, California. Geology 28, 983–986.
Stuwe, K., Hintermuller, M., 2000. Topography and isotherms revisited: the influence of laterally migrating drainage divides. Earth Planet. Sci. Lett. 184, 287–303.
Stuwe, K., White, L., Brown, R., 1994. The influence of eroding topography on steady-state isotherms — application to fission-track analysis. Earth Planet. Sci. Lett. 124, 63–74.
Tang, Q.Y., Zhang, M.J., Li, X.Y., Li, L.W., He, P.P., Lin, Y., 2012. The chemical and carbon isotopic compositions of volatiles in Cenozoic high-potassic basalts in western Qinling, China and their mantle geodynamic implications. Acta Petrol. Sin. 28, 1251–1260.
Tapponnier, P., Molnar, P., 1977. Active faulting and tectonics in China. J. Geophys. Res. 82, 2905–2930.
Tapponnier, P., Xu, Z.Q., Roger, F., Meyer, B., Arnaud, N., Wittlinger, G., Yang, J.S., 2001. Oblique stepwise rise and growth of the Tibet plateau. Science 294, 1671–1677.

van der Meer, D.G., Spakman, W., van Hinsbergen, D.J.J., Amaru, M.L., Torsvik, T.H., 2010. Towards absolute plate motions constrained by lower-mantle slab remnants. Nat. Geosci. 3, 36–40.
Wagner, G.A., Reimer, G.M., 1972. Fission track tectonics: the tectonic interpretation of fission track apatite ages. Earth Planet. Sci. Lett. 14, 263–268.
Wang, D.Z., Shu, L.S., Faure, M., Sheng, W.Z., 2001. Mesozoic magmatism and granitic dome in the Wugongshan Massif, Jiangxi province and their genetical relationship to the tectonic events in southeast China. Tectonophysics 339, 259–277.
Wang, E., Kirby, E., Furlong, K.P., van Soest, M., Xu, G., Shi, X., Kamp, P.J.J., Hodges, K.V., 2012. Two-phase growth of high topography in eastern Tibet during the Cenozoic. Nat. Geosci. 5, 640–645.
Wong, W.H., 1927. Crustal movements and igneous activities in eastern China since Mesozoic times. Bull. Geol. Soc. China 6, 9–37.
Wong, W.H., 1929. The Mesozoic orogenic movement in eastern China. Bull. Geol. Soc. China 8, 33–44.
Wu, G.Y., 2005. The Yanshanian orogeny and two kinds of yanshanides in Eastern-Central China. Acta Geol. Sin. 79, 507–518.
Xiao, P.X., Zhang, J.Y., Wang, H.L., Lei, H.Y., 2000. Subdivision of rock series units and determination of intrusion age of Taibai rock mass in North Qinling. Northwest Geosci. 21, 37–48.
Xing, Z.Y., Zhao, B., Tu, M., 2005. The formation of the Fenweirift Valley (in Chinese). Earth Sci. Front. 12, 247–262.
Xu, P., Zhao, D., 2009. Upper-mantle velocity structure beneath the North China Craton: implications for lithospheric thinning. Geophys. J. Int. 177, 1279–1283.
Yang, J.H., Wu, F.Y., Shao, J.A., Wilde, S.A., Xie, L.W., Liu, X.M., 2006. Constraints on the timing of uplift of the Yanshan Fold and Thrust Belt, North China. Earth Planet. Sci. Lett. 246, 336–352.
Ye, H.S., Mao, J.W., Li, Y.F., Guo, B.J., Zhang, C.Q., Liu, W.J., Yan, Q.R., Liu, G.Y., 2006. SHRIMP zircon U–Pb and molybdenite Re–Os dating for the superlarge Donggou porphyry Mo deposit in East Qinling, China, and its geological implication. Acta Geol. Sin. 80, 1078–1088.
Yin, A., 2010. Cenozoic tectonic evolution of Asia: a preliminary synthesis. Tectonophysics 488, 293–325.
Yin, A., Harrison, T.M., 2000. Geologic evolution of the Himalayan–Tibetan orogen. Annu. Rev. Earth Planet. Sci. 28, 211–280.
Yin, A., Nie, S.Y., 1993. An indentation model for the North and South China collision and the development of the Tan–Lu and Honam Fault Systems, eastern Asia. Tectonics 12, 801–813.
Yin, G.M., Lu, Y.C., Zhao, H., Li, W.L., Li, L., Guo, S.L., 2001. The tectonic uplift of the Hua Shan in the Cenozoic. Chin. Sci. Bull. 46, 1665–1668.
Yuan, Y.S., Hua, S.B., Wang, H.J., Sun, F.J., 2007. Meso-Cenozoic tectonothermal evolution of Ordos basin, central China: insights from newly acquired vitrinite reflectance data and a revision of existing paleothermal indicator data. J. Geodyn. 44, 33–46.
Zhang, K.J., 2013. Lithosphere folding-induced removal of lithospheric mantle? J. Geodyn. 53, 8–17.
Zhang, G., Yu, Z., Sun, Y., Cheng, S., Li, T.D., Xue, F., Zhang, C., 1989. The major suture zone of the Qinling orogenic belt. J. Southeast Asian Earth Sci. 3, 63–76.
Zhang, A.L., Yang, Z.T., Zhong, J., Mi, F.S., 1995. Characteristics of late Quaternary activity along the southern border fault zone of Weihe graben basin. Quat. Int. 25, 25–31.
Zhang, Y.Q., Mercier, J.L., Vergely, P., 1998. Extension in the graben systems around the Ordos (China), and its contribution to the extrusion tectonics of south China with respect to Gobi–Mongolia. Tectonophysics 285, 41–75.
Zhang, G.W., Zhang, B.R., Yuan, X.C., Xiao, Q.H., 2001. Qinling Orogenic Belt and Continental DynamicsScience Press, Beijing.
Zhang, K.J., Zhang, Y.X., Tang, X.C., Xia, B., 2012. Late Mesozoic tectonic evolution and growth of the Tibetan Plateau prior to the Indo-Asian collision. Earth Sci. Rev. 114, 236–249.
Zheng, D.W., Zhang, P.Z., Wan, J.L., Li, D.M., Wang, F., Yuan, D.Y., Zhang, G.L., 2004. The $^{40}Ar/^{39}Ar$, fission track evidence of Mesozoic tectonic in northern margin of west Qinling mountain. Acta Petrol. Sin. 20, 697–706.
Zheng, T.Y., Chen, L., Zhao, L., Xu, W.W., Zhu, R.X., 2006. Crust–mantle structure difference across the gravity gradient zone in North China Craton: seismic image of the thinned continental crust. Phys. Earth Planet. Inter. 159, 43–58.
Zhisheng, A., Kutzbach, J.E., Prell, W.L., Porter, S.C., 2001. Evolution of Asian monsoons and phased uplift of the Himalayan Tibetan Plateau since Late Miocene times. Nature 411, 62–66.
Zhou, D.W., Zhao, Z.Y., Li, Y.D., 1994. Geological Features Along the Southwest Margin of the Ordos Basin and the Relations to the Evolution of the Qinling Orogen. Geological Publishing House, Beijing.
Zhu, M., 1995. The ages of K–Ar isochron and 39Ar–40Ar of granites from Qinling area and their geological significance. Acta Petrol. Sin. 11, 179–192.
Zhu, L.M., Zhang, G.W., Guo, B., Li, B., 2008. U–Pb (LA-ICP-MS) zircon dating for the large Jinduicheng porphyry Mo deposit in the East Qinling, China, and its metallogenetic geodynamical setting. Acta Geol. Sin. 82, 204–220.